Materials Horizons

ROYAL SOCIETY OF CHEMISTRY

REVIEW

View Article Online
View Journal

Check for updates

Cite this: DOI: 10.1039/d5mh01556a

Clean production of chlorine (Cl_2) and hypochlorous acid (HOCl) from photocatalytic and photoelectrochemical seawater splitting

Rohul H. Adnan *[a][b] and Yun Hau Ng *[a][b]

Seawater splitting has emerged as a promising alternative to overall water splitting because it eliminates the kinetically sluggish oxygen evolution reaction (OER), which is a bottleneck in water splitting, and avoids the low economic value of O_2. Moreover, in seawater splitting, H_2 evolution coupled with the oxidation of chloride (Cl^-) to value-added chlorine (Cl_2) and/or hypochlorous acid (HOCl) can simultaneously benefit the energy and environmental sectors. Cl_2 and HOCl are widely used for bleaching, disinfection, sanitisation and sterilisation in the medical sector and for purifying drinking water and water in swimming pools owing to their strong oxidising and antibacterial properties. Mainstream industrial production employs the chlor-alkali electrolysis of sodium chloride (NaCl), which requires significant energy input and releases enormous amounts of CO_2. To achieve the sustainable production of Cl_2 and HOCl while reducing energy consumption and environmental impacts, photocatalytic (PC) and photoelectrochemical (PEC) technologies have been employed as green alternatives. Importantly, PC and PEC enable the on-site production of Cl_2/HOCl in remote areas, which can circumvent their instability (decomposition), storage and transport issues. This article reviews the recent progress in the PC and PEC production of Cl_2/HOCl, along with the catalytic materials used and their designs and photocatalytic performance. The applications of *in situ* HOCl production in anti-bacterial treatment, ammonia removal, the selective oxidation and conversion of organic compounds, and CO_2 conversion are discussed. We also address the challenges in this area and highlight prospects for future research directions. Overall, we demonstrate that the PC and PEC production of Cl_2/HOCl serves as a green and sustainable alternative to the chlor-alkali process. This research area is still in its infancy, and we hope that this review article will garner the attention of researchers to contribute to this area, leading to a step closer toward practical applications.

Received 13th August 2025,
Accepted 30th January 2026

DOI: 10.1039/d5mh01556a

rsc.li/materials-horizons

Wider impact

The chlor-alkali process has been the predominant industrial production process for chlorine gas (Cl_2) *via* the electrolysis of seawater since 1892. Despite its industrial success, the large energy input, high capital costs, complex separation and purification processes, and toxic cell components (mercury in mercury cells and asbestos in diaphragm cells) have led to serious energy and environmental concerns. The most straightforward path to clean and sustainable production of Cl_2/HOCl is by employing a solar-to-chemical conversion mechanism. Progress in photocatalytic (PC) and photoelectrochemical (PEC) technologies has achieved maturity, yet their application in Cl_2/HOCl production is still in its infancy. PC and PEC technologies harvesting solar energy and using seawater in the presence of suitable photocatalysts are expected to reduce energy input and environmental impacts. Moreover, these technologies enable on-site production of Cl_2/HOCl in remote areas using portable PC and PEC cells, which can overcome the instability, transport, and storage issues of Cl_2/HOCl. This review discusses the recent progress in the PC and PEC production of Cl_2/HOCl from seawater splitting in the past decade. Importantly, the oxidation of chloride (Cl^-) at the anode (or anodic site) can be coupled with hydrogen production or CO_2 reduction at the cathode (or cathodic site) for the simultaneous production of fuels and useful chemicals as a type of artificial photosynthesis.

1. Introduction

The two most pressing long-standing global challenges are the energy crisis due to the depletion of fossil fuels and environmental pollution resulting from human activities, industrial

---

[a] *Center for Renewable Energy and Storage Technologies (CREST), Physical Science and Engineering (PSE) Division, King Abdullah University of Science and Technology (KAUST), Thuwal 23955-6900, Saudi Arabia. E-mail: rohul.adnan@kaust.edu.sa, yunhau.ng@kaust.edu.sa*

[b] *Clean Energy Research Platform (CERP), Physical Science and Engineering (PSE) Division, King Abdullah University of Science and Technology (KAUST), Thuwal 23955-6900, Saudi Arabia*

chemical processes and power plants. Therefore, there is an urgency to implement renewable energy strategies, including wind energy, photovoltaic solar cells and H_2 production, to mitigate these issues. H_2 production *via* photocatalytic water splitting has been dominating the photocatalysis research for the last 50 years since the groundbreaking work by Honda and Fujishima.[1,2] Despite extensive research efforts, photocatalytic water splitting is far from practical realisation due to the challenging issues like the reverse reaction of H_2 and O_2, slow kinetics of O_2 evolution reaction (OER), and low solar-to-hydrogen (STH) efficiency ($<10\%$).[2] A recently proposed strategy is to couple the H_2 evolution reaction (HER) with more kinetically favourable oxidation reactions that produce high value-added compounds to circumvent the issues of the slow kinetics of the OER and the low economic value of O_2.[3–5] Sayama has pioneered the photoelectrochemical oxidation of several high value-added chemicals, including H_2O_2, HOCl, $S_2O_8{}^{2-}$ and Ce^{4+}, paving the way towards the effective utilization of solar light energy and oxidative power of photogenerated holes.[6] Chloride (Cl^-) oxidation to Cl_2 and/or HOCl proceeds smoothly in a seawater solution, allowing the use of abundant and low-cost seawater/saltwater. To the best of our knowledge, photocatalytic seawater splitting has not been extensively discussed in the literature, and therefore, it is timely to present a comprehensive review on photocatalytic (PC) and photoelectrochemical (PEC) seawater splitting.

Hypochlorous acid (HOCl) and sodium hypochlorite (NaOCl) are widely used in a plethora of applications in industrial processes and commercial applications, including pulp and paper bleaching, sanitization, and wound care.[7] For use in bleaching and disinfection, 40% of the application goes into drinking water and wastewater treatments, and the remaining 60% is used in household applications, including pool sanitization, laundry bleaching and surface disinfection, in food processing and healthcare facilities. The most common type of drinking water disinfection is chlorination, which is highly effective in killing bacteria and other microorganisms to ensure that the water is safe for drinking. The World Health Organization (WHO) has set the recommended Cl_2 concentration to 2 mg L^{-1} for effective household water treatment and the residual free Cl_2 to 0.2–0.5 mg L^{-1}.[8] For convenience, Cl_2, HOCl and ClO^- are classified as reactive chlorine species (RCS) and are used throughout this article although sometimes they are termed HOCl in other articles.[9,10] RCS are produced commercially on a large-scale using the chlor-alkali electrochemical process in a brine (NaCl) solution. However, due to the uphill thermodynamic process and formation of unwanted species, the electricity consumption in the chlor-alkaline process is huge, which leads to enormous CO_2 emissions, thus resulting in a significant reduction in energy consumption and carbon footprint using green and sustainable alternatives.[11] In light of energy-efficient processes and reduced environmental impacts, photocatalytic (PC) and photoelectrochemical (PEC) technologies pave the way towards a green and sustainable strategy for the production of RCS.

In water splitting, O_2 is produced along with H_2 (eqn (1)). However, the oxygen evolution reaction (OER) has become a kinetic bottleneck due to its large overpotential. Moreover, from a practical point of view, O_2 has a negligible economic value. In saltwater/seawater, Cl^- ions are present in the majority, and the Cl^- oxidation reaction (COR) *via* a two-electron process is more kinetically favourable than the OER due to the lower overpotential. The use of seawater can dramatically reduce the operating costs of PC or PEC water splitting, where pure water is very scarce and expensive. In the chlor-alkali process, Cl^- is oxidized at the anode to form Cl_2 (eqn (3)), and dissolved Cl_2 in water forms hypochlorous acid (HOCl) *via* a disproportion reaction (eqn (4)) or is mixed with sodium hydroxide (NaOH) to form NaOCl. The distribution of Cl_2, HOCl and OCl^- in aqueous solution depends on the pH of the solution. Under acidic, neutral and basic conditions, Cl^- is oxidized to Cl_2, HOCl and OCl^-, respectively (Fig. 1a).[12] HOCl exists in equilibrium with molecular Cl_2 (eqn (6)). If Cl_2 is allowed to escape, the equilibrium shifts to the left, reducing the amount of HOCl. Therefore, the selectivity of RCS for Cl^- oxidation depends on the complexity of the pH-dependent equilibria of the solution. Fig. 1b shows the Pourbaix diagram of the chlorinated species across all pH values. Nonetheless, it is difficult to maintain the stability of HOCl because of its rapid decomposition even in the dark. The decomposition of HOCl

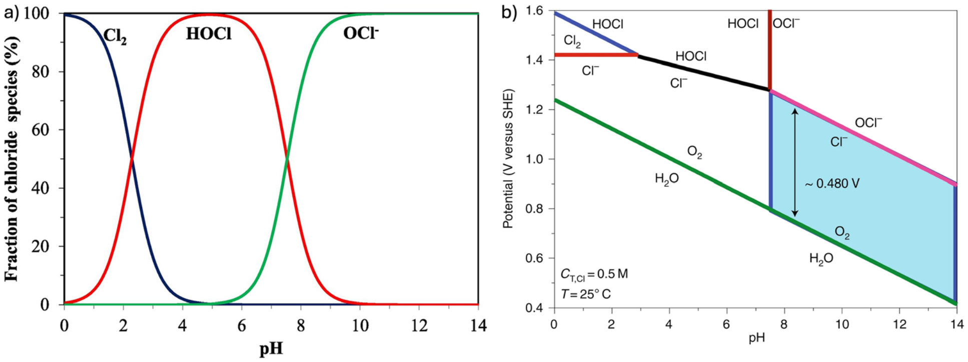

Fig. 1 (a) Distribution of reactive chlorine species (RCS) of Cl_2, HOCl, and ClO^- across a wide pH range from acidic to neutral and basic. Reproduced from ref. 14. Copyright 2020, Elsevier. (b) Pourbaix diagram of the reactive chlorine species at all pH values. Reproduced from ref. 15. Copyright 2025, Springer.

follows two disproportionate pathways, producing either chlorate and/or oxygen (refer to Section 2 for details).[13] Such rapid decomposition makes on-site production of HOCl *via* PC or PEC even more compelling to avoid the need for long-distance transport and long-term storage.

$$2H^+ + 2e^- \rightarrow H_2 \quad E = 0\ \text{V}\ vs.\ \text{RHE} \tag{1}$$

$$O_2 + 4H^+ + 4e^- \rightarrow 2H_2O \quad E = -1.23\ \text{V}\ vs.\ \text{RHE} \tag{2}$$

$$2Cl^-(aq) \rightarrow Cl_2(g) + 2e^- \quad E = 1.36\ \text{V}\ vs.\ \text{RHE} \tag{3}$$

$$Cl^- + H_2O \rightarrow HOCl + H^+ + 2e^- \quad E = 1.49\ vs.\ \text{RHE} \tag{4}$$

$$Cl^- + H_2O \rightarrow OCl^- + 2H^+ + 2e^- \quad E = 1.72\ \text{V}\ vs.\ \text{RHE} \tag{5}$$

$$Cl_2 + H_2O \rightleftharpoons H^+ + Cl^- + HOCl \tag{6}$$

$$HOCl \rightleftharpoons H^+ + OCl^- \tag{7}$$

A photocatalytic process requires a suitable photocatalyst, a Cl-saturated solution and light to produce Cl_2 and/or HOCl. The sources of Cl^- include a brine solution, aqueous HCl, and seawater/saltwater. Seawater is an ideal and practical reaction solution due to its abundance, cost-effectiveness, and unlimited availability compared to pure water, which incurs an additional cost for its high-purity resource. Most ions in seawater are Cl^- (55%), followed by sulfate (SO_4^{2-}, 7.7%) and carbonate (CO_3^{2-}, 0.33%). For this reason, a seawater solution for photocatalytic HOCl or Cl_2 production is often used at 0.5–0.6 M (or 3.5 wt%) aqueous NaCl to mimic natural seawater.[16] Therefore, the photocatalytic Cl^- oxidation reaction (COR) brings about four merits: (i) the use of renewable solar energy, (ii) a low-cost and low carbon footprint process, (iii) on-demand production for remote areas, and (iv) no requirement for facilities for storage, handling and transport of RCS. Notably, the simultaneous PC production of H_2 and HOCl avoids the use of an expensive membrane due to self-separation by phase (gaseous H_2 *vs.* liquid HOCl). Additionally, a seawater solution can be an ideal, low-cost electrolyte for operating PEC cells.

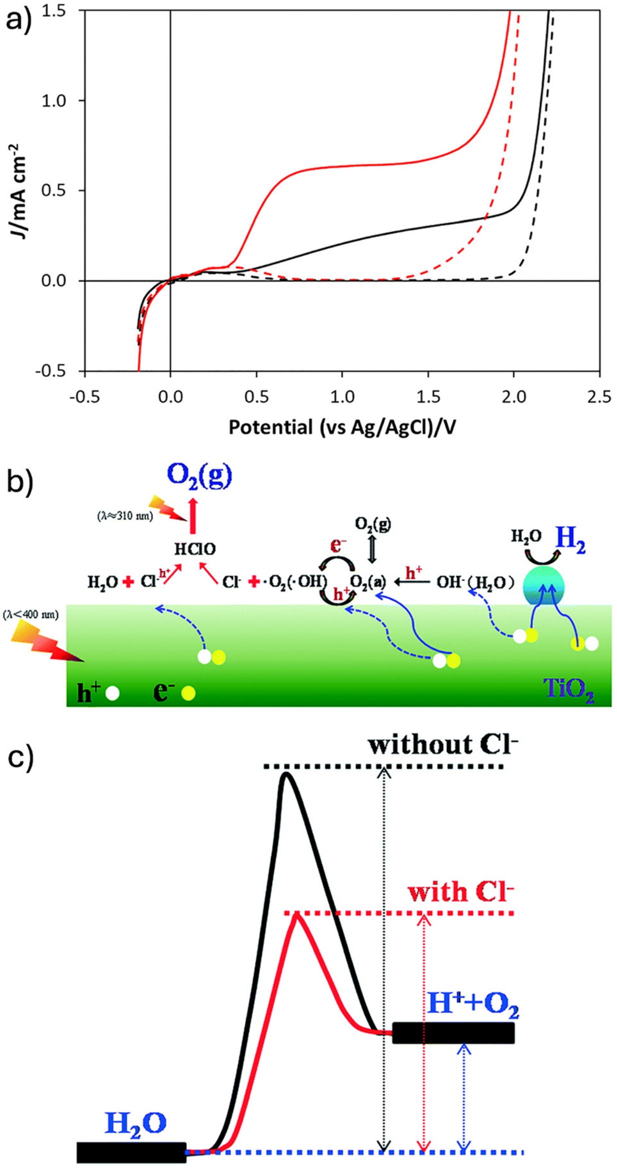

Fig. 2 (a) Photocurrent density of water (black) and Cl^- (red) oxidation. Reproduced from ref. 18. Copyright 2023, the Royal Society of Chemistry. (b) Mechanism of seawater splitting into H_2 and O_2 through the formation of an HOCl intermediate in the presence of Cl^-. (c) Free energy diagram of seawater splitting. Reproduced from ref. 17. Copyright 2014, the Royal Society of Chemistry.

For Cl^- to be oxidized to Cl_2 by a photogenerated hole, the valence band (VB) must be more positive than 1.36 V (*vs.* RHE). This redox potential is not significantly different from that of water oxidation to O_2 potential (1.23 V *vs.* RHE); therefore, Cl^- oxidation usually competes with water oxidation. In seawater or seawater solution, Cl^- oxidation is preferred to water oxidation due to a large overpotential (∼0.25 V) and thus sluggish kinetics of the latter.[17] As an example, Johnston's group recorded a current density in $HClO_4$ and NaCl/$HClO_4$ electrolytes and observed a twice higher current density for Cl^- oxidation compared to that of water oxidation between 0.5 and 2.0 V (Fig. 2a).[18] Moreover, it has been shown that Cl^- can quench a photogenerated hole, giving an advantage of selective HOCl formation over water oxidation.[19,20] In some work, it has been shown that O_2 evolution in saltwater/seawater originates from the decomposition of HOCl, providing a kinetically easier route for O_2 evolution than direct 4-electron water oxidation.[9] Notably, Huang *et al.* unravelled that adding a small amount of Cl^- in water or pre-adsorbing Cl^- on TiO_2 lowered the activation barrier, thereby boosting the H_2 production rate by 3-fold and achieving a stoichiometric ratio of H_2 and O_2 evolution in water splitting (Fig. 2b and c).[17] Similarly, enhanced H_2 production using a p-GaN-based nanowire in seawater (*cf.* pure water) is attributed to Cl^- oxidation and better conductivity of seawater.[21] These works also suggest that seawater splitting is a feasible strategy for improving water splitting for a high production rate of H_2. Although this article focuses exclusively on the production of Cl_2/HOCl *via* PC and PEC seawater splitting, readers interested in photocatalytic H_2

production from seawater splitting are encouraged to refer to related review articles elsewhere.[22–24]

With growing attention in this research area over the past decade, it is timely to present a comprehensive and critical discussion on the development of the effective production of Cl_2/HOCl. This review article aims to discuss the recent progress in PC and PEC of Cl_2/HOCl production and review the photocatalytic materials and designs, as well as their photocatalytic performance. First, we present an overview of the challenges in the effective production of Cl_2 and HOCl. Next, we review the photocatalytic materials designed for this purpose, including metal oxides, metal chloride and oxychlorides. In addition, we highlight the applications of photocatalytic HOCl production in other related areas, including antibacterial treatment, degradation of ammonia–nitrogen, selective oxidation and conversion of organic compounds, and photocatalytic CO_2 reduction. Given the rapid progress in this area, it is appropriate and meaningful to summarise the developments in PC and PEC material designs for Cl_2/HOCl production. We believe that this timely review will guide catalytic researchers, materials scientists and computational chemists in catalytic materials designs and developments for industrially relevant processes.

2. Challenges in Cl_2 and HOCl production

Low Cl_2 and HOCl yields

Low yields and selectivity of Cl_2 and HOCl formation result from a few factors. First, further oxidation of Cl_2 or HOCl to higher chlorine oxo species, like ClO_2^-, ClO_3^-, and ClO_4^-, under UV irradiation, which are usually toxic, is shown in eqn (8)–(10).[25,26] Formation of higher chlorine oxo species over a prolonged reaction time leads to the reduction of faradaic efficiency (FE).

$$Cl^- + 2H_2O \rightarrow ClO_2^- + 4H^+ + 4e^- \quad E^0 = 0.76 \ vs. \ \text{RHE} \tag{8}$$

$$Cl^- + 3H_2O \rightarrow ClO_3^- + 6H^+ + 6e^- \quad E^0 = 1.45 \ vs. \ \text{RHE} \tag{9}$$

$$Cl^- + 4H_2O \rightarrow ClO_4^- + 8H^+ + 8e^- \quad E^0 = 1.39 \ vs. \ \text{RHE} \tag{10}$$

Second, Cl_2 dissolves in water to produce HOCl and HCl (refer to eqn (6)). HOCl has a limited stability and forms radicals, like $^\bullet OH$ and $^\bullet Cl$, upon exposure to UV light irradiation (eqn (11)).[27–29] In the presence of $^\bullet OH$, it reacts with HOCl to generate $^\bullet OCl$ and consequently to reduce the HOCl yield.[30] HOCl can also decompose to yield O_2 (eqn (12)) as discussed in the previous section. As a result, the use of wide band gap semiconductors like ZnO and TiO_2, which absorb UV light, poses a problem for Cl_2/HOCl formation. Notably, the deep valence band maximum for some semiconductor photocatalysts underscores their strong oxidising capability to decompose Cl_2 and HOCl.[31] In addition, there is evidence of HOCl or OCl^- decomposition to ClO_3^- and Cl^- under UV (365 nm LED) irradiation, as reported by Okada *et al.*, reducing the overall yield of HOCl (eqn (13)).[32] As a matter of fact, Koo *et al.* showed that the formation of toxic ClO_3^- can be inhibited using visible light instead of UV light in PEC systems.[30]

Decomposition of HOCl

$$\text{HOCl} \xrightarrow{\lambda < 400\text{nm}} {}^\bullet\text{OH} + {}^\bullet\text{Cl} \tag{11}$$

$$\text{HOCl} \xrightarrow{\lambda < 400\text{nm}} \frac{1}{2}O_2 + H^+ + Cl^- \tag{12}$$

$$3OCl^- \xrightarrow{\lambda = 365\ \text{nm}} ClO_3^- + 2Cl^- \tag{13}$$

For immediate applications, such as pollutant degradation or oxidative organic reactions using *in situ* generated Cl_2 and/or HOCl, rapid decomposition to radicals is highly favoured because they are responsible for oxidising pollutants. Similarly, *in situ*-generated O_2 from HOCl decomposition might serve as an oxidant in oxidation reactions. Although short-lived HOCl seems like a drawback owing to its high-yield production, its use in wastewater or sewage treatment and organic transformation is a merit. A discussion on the photodegradation of pollutants and bacteria, and the photocatalytic conversion of organic compounds, is provided in Section 7.

The need for O_2 supply

It has been found that the presence of O_2 for ORR is required to achieve a high production rate of HOCl in Cl^- oxidation. Molecular O_2 acts as an electron scavenger to suppress the recombination of charge carriers so that holes can be consumed by Cl^- ions for the chloride oxidation reaction (COR). For some photocatalysts, like BiOCl, molecular O_2 is required to prevent self-reduction of lattice Bi^{3+} to lower oxidation states, *e.g.* Bi metal. Nonetheless, the need for a constant supply of O_2 may restrict the feasibility of the green strategy in photocatalytic Cl_2/HOCl production. Additionally, CO_2 has also been found to quench electrons, leading to the coupling of the photoreduction of CO_2 and the photooxidation of Cl^- ions as a means of producing fuels and oxidants in a single photocatalytic system. Therefore, the use of natural seawater containing a decent amount of dissolved CO_2 might be an advantage for COR.

Photocorrosion and dissolution of catalytic materials

Another issue is the dissolution and/or photocorrosion of photocatalytic materials in a neutral seawater solution or seawater. The production of Cl_2 and HOCl leads to local acidification, which changes the pH of the seawater solution to become acidic (refer to eqn (6)). Jadwiszczak *et al.* calculated the pH of 0.5 M NaCl to be 2.5 upon Cl_2 evolution and dissolution.[33] Although some photocatalytic materials, like WO_3, TiO_2 and $BiVO_4$, are chemically stable in an acidic medium, other materials such as Cu_2O and CdS undergo photocorrosion upon exposure to light for a prolonged duration. Furthermore, although metal co-catalysts dramatically enhance the production rate and yield of Cl_2/HOCl, their use in acidic media has limited stability. For instance, Okada *et al.* observed a partial dissolution of Pt co-catalyst in acidic seawater solution at pH 1 after one hour of photocatalysis; it must be noted that the dissolution of Pt only occurs under photoirradiation.[32] Therefore, modifications to photocatalysts and photoanodes are often required to preserve stability in the presence of Cl^- ions under highly oxidising conditions (Cl_2 and HOCl) and/or under photoirradiation. For example, a MoO_x layer is inserted between $Co_2(OH)_3Cl$ and $BiVO_4$ to suppress the photocorrosion of $Co_2(OH)_3Cl$ by photogenerated holes of $BiVO_4$.[34]

Complex mixture of natural seawater

Natural seawater is an ideal reaction medium owing to its abundance and free availability. Although natural seawater contains Cl^- ions as a majority, the presence of other cations (Na^+, Ca^{2+}, Mg^{2+}, and Ba^{2+}) and anions (HCO_3^-, CO_3^{2-}, and SO_4^{2-}) interferes with the surface of photocatalysts by selective adsorption and reaction, thereby reducing the overall production yield and rate of HOCl. Some of these ions, like CO_3^{2-}, SO_4^{2-} and PO_4^{3-}, are effective hole scavengers that compete with Cl^- oxidation, thereby reducing its selectivity.[35] Additionally, HCO_3^-, CO_3^{2-}, and PO_4^{3-} have been shown to consume Cl_2/HOCl.[36] Furthermore, the adsorption of these ions on the surface of photocatalysts might block the diffusion and interaction of Cl^- with the surface. Therefore, the deleterious effects of these ions are inevitable. As a result, designing photocatalytic materials that can perform efficiently in seawater containing various ions, as opposed to pure seawater solutions, is a major challenge in this research area. The average composition of natural seawater is summarized in Table 1.

Table 1 Percentage composition of ions in natural seawater[37,38]

Ion	Composition (%)
Cl^-	55
Na^+	31
SO_4^{2-}	7.7
Mg^{2+}	3.7
Ca^{2+}	1.2
K^+	1.1
HCO_3^-	0.3
Br^-	0.2
CO_3^{2-}	0.03
Sr^{2+}	0.03
Other ions	0.09

3. Mechanism of Cl_2 formation

Although Cl^- oxidation to Cl_2 looks like a simple 2-electron oxidation process, this mechanism is still under debate. Three mechanistic reaction pathways have been proposed based on theoretical calculations and experimental electrochemical studies: Volmer–Tafel, Volmer–Heyrovsky and Krishatalik.[39]

Volmer–Tafel

$$2Cl^- + 2{*} \rightarrow 2Cl{*} + 2e^- \tag{14}$$

$$Cl{*} + Cl{*} \rightarrow 2{*} + Cl_2 \tag{15}$$

Volmer–Heyrovsky

$$2Cl^- + {*} \rightarrow Cl{*} + Cl^- + e^- \tag{16}$$

$$Cl^- + Cl{*} \rightarrow {*} + Cl_2 + e^- \tag{17}$$

Krishatalik

$$2Cl^- + {*} \rightarrow Cl{*} + Cl^- + e^- \tag{18}$$

$$Cl^- + Cl{*} \rightarrow Cl{*}^+ + Cl^- + e^- \tag{19}$$

$$Cl^- + Cl{*}^+ \rightarrow {*} + Cl_2 \tag{20}$$

where * represents the active sites, *e.g.* metal atoms or surface oxygen. In all the proposed pathways, a Cl^- ion is oxidised at the active site (*), forming adsorbed Cl* species. In the Volmer–Tafel mechanism, two Cl* species combine and are released from the surface of the electrode as Cl_2. However, in Volmer–Heyrovsky, Cl* reacts with a Cl^- ion to form Cl_2. The Krishatalik mechanism requires three steps for the formation of Cl_2 through the reaction between a Cl^- ion and $Cl{*}^+$ species.

Three possible reaction pathways have been proposed based on theoretical computations, kinetic data and experimental verifications as plausible mechanisms. The elementary steps in COR are Volmer, Tafel, and Heyrovsky. The adsorption of Cl^- on the active site of an electrode is termed the Volmer step. The Tafel step includes a combination of two adsorbed Cl* species forming a Cl_2 product. The formation and desorption of a product following a reaction between an adsorbed species (Cl*) and a reactant (Cl^-) is called the Heyrovsky step. In the Krishtalik step, a second electron transfer occurs between a reactant and an adsorbed species prior to product formation. The three mechanistic pathways are illustrated in Fig. 3.

Herein, we discuss the mechanism of the chlorine evolution reaction (CER) using a RuO_2 model system, one of the best performing catalysts for the chlor-alkali process. The mechanistic reaction pathway is often proposed based on kinetic experimental data. However, kinetic data alone do not provide the nature of the active sites of a catalyst and intermediates. Moreover, the nature of the active sites has not been elucidated by *in situ* spectroscopy. Exner *et al.* performed *ab initio* atomistic thermodynamic calculations on the model catalyst O-covered $RuO_2(110)$.[41] Electrochemical adsorption (Volmer step) of Cl^- on the fully O-covered $RuO_2(110)$ surface at electrode potential, $U = 0$ V, costs a Gibbs energy change of 1.49 eV. In the Volmer–Heyrovsky mechanism, a direct reaction between an adsorbed chlorine (Cl*) and a chloride (Cl^-) from the solution to yield gaseous Cl_2 requires a Gibbs energy change of 1.23 and −0.13 eV at $U = 0$ V and 1.36 V, respectively. The net Gibbs energy loss in the Volmer–Heyrovsky mechanism is 0.13 eV. Meanwhile, the second Cl^- adsorption in the Volmer–Tafel mechanism requires a Gibbs energy change of 1.59 and 0.23 eV at $U = 0$ V and 1.36 V, respectively. Therefore, the Gibbs energy loss is 0.23 eV in the Volmer–Tafel mechanism. The formation of a Cl^+ ion in the Krishtalik mechanism results in a Gibbs energy loss of 0.85 eV, which is much higher than the Volmer–Heyrovsky and Volmer–Tafel mechanisms. Hence, the Krishtalik mechanism can be ruled out for CER on the fully

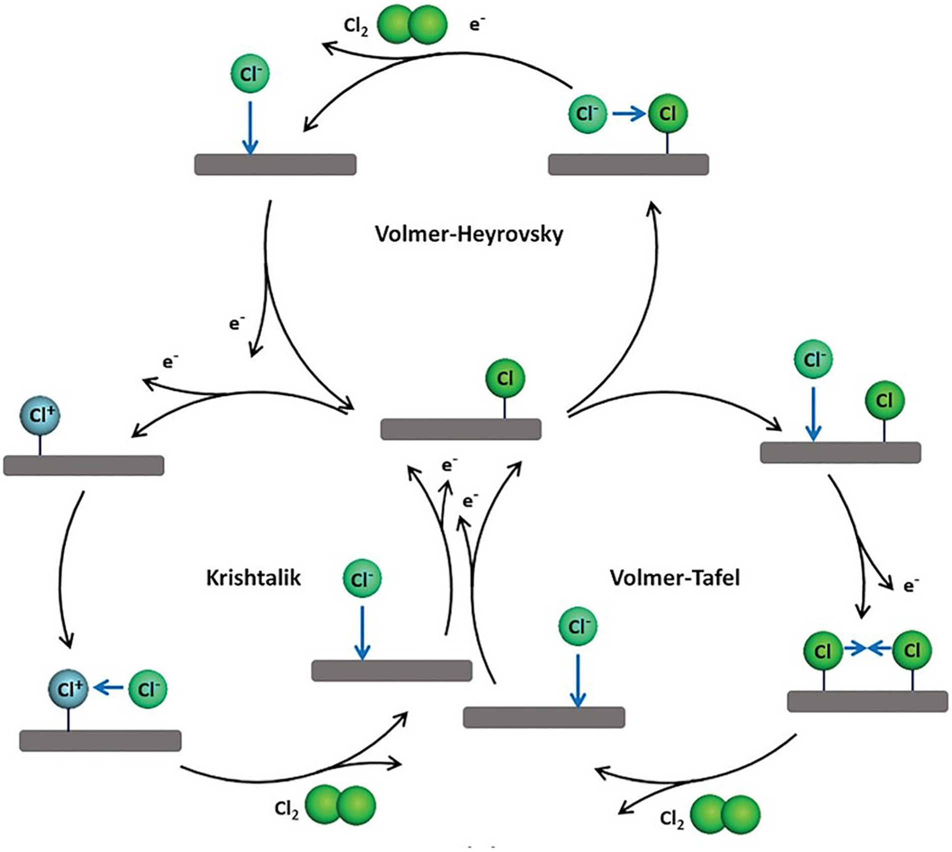

Fig. 3 Scheme of the mechanistic pathways for chloride oxidation according to the mechanisms of Volmer–Heyrovsky, Volmer–Tafel, and Krishtalik. Reproduced from ref. 40. Copyright 2023, Wiley-VCH.

O-covered $RuO_2(110)$ surface while favouring Volmer–Heyrovsky as the most plausible mechanism based on thermodynamic considerations. Additionally, doping a monolayer of PtO_2 in $RuO_2(110)$ further lowers the Gibbs energy loss of 0.08 eV. Importantly, it should be noted that while the Volmer–Heyrovsky mechanism is the most plausible and preferred pathway, all proposed mechanistic pathways are feasible on the $RuO_2(110)$ surface.[39] The simplified mechanism of Volmer-Heyrovsky on metal oxides (MOs) is given by

$$\text{M–O} + \text{Cl}^- \rightarrow \text{M–OCl} + e^- \quad (21)$$

$$\text{M–OCl} + \text{Cl}^- \rightarrow \text{M–O} + \text{Cl}_2 + e^- \quad (22)$$

In a previous study, Khrishtalik proposed a three-elementary step mechanism following a combination of electrochemical measurements and electrokinetic data on RuO_2–TiO_2.[42] A combination of a low coverage of intermediate and a low slope of the anodic polarisation curve provides a strong indication that the transfer of the first electron is reversible and the second electron transfer is a slow step. A total of two electrons per one Cl^- is consumed in the slow step, suggesting that a positive Cl (Cl^+) should react with a chloride (Cl^-) to form Cl_2. Khristalik then proposed a mechanism with three elementary steps (eqn (18)–(20)) for CER. Although this proposed mechanism based on electrokinetic data and electrochemical measurements seems plausible, it certainly does not provide a correlation with the physical and structural characteristics of electrocatalysts, a limitation that must be addressed to gain a correct understanding of CER selectivity on the electrode surface. Furthermore, the microscopic molecular level of insights is not captured and elucidated by electrokinetic data, which often requires computational calculations, such as *ab initio* DFT with thermodynamic considerations/frameworks. DFT calculations by Hansen *et al.* on chlorine evolution disclosed the possibility of Cl^- adsorption on two oxygen atoms in $RuO_2(110)$, forming ClO_2^{cc} (cc denotes two coordinatively unsaturated sites).[43] This result, in which ClO_2^{cc} is more positively charged than O_2^{cc}, is consistent with the Khrishtalik mechanism.

4. Detection and determination of Cl_2 and HOCl concentrations

The photocatalytic activity in Cl^- oxidation is assessed using the production rate and/or concentration of Cl_2 or HOCl. The concentration of Cl_2 in seawater splitting can be quantified using iodometric titration. The iodide-starch test is usually employed where iodide is oxidised to iodine in the presence of Cl_2 as an oxidising agent, following eqn (23). The generated iodine is titrated with sodium thiosulfate using starch as a colour indicator to determine the concentration of iodine (eqn (24)), and thus Cl_2 indirectly.[44]

$$Cl_2 + 2I^- \rightarrow I_2 + 2Cl^- \tag{23}$$

$$I_2 + 2S_2O_3^{2-} \rightarrow 2I^- + S_4O_6^{2-} \tag{24}$$

The evolved Cl_2 can also be detected using the *N*,*N*′-bis(2,4-di-sulfobenzyl)tolidine tetrasodium method. Briefly, Cl_2 is purged from a photoreactor under an inert gas flow and trapped in a 4 M aqueous NaOH solution to form hypochlorite (ClO^-) ions, and the amount of ClO^- is determined using *N*,*N*′-bis(2,4-di-sulfobenzyl)tolidine tetrasodium (SBT).[32] The oxidized form of SBT following a reaction with chlorine has a characteristic absorption at 675 nm at pH 5.2, which allows a spectroscopic detection.[45] The concentration of HOCl is commonly determined spectroscopically using the *N*,*N*-diethyl-*p*-phenylenediamine (DPD) method. In the presence of HOCl, DPD is oxidized to a red species with characteristic absorption at 515 or 552 nm.

The selectivity for Cl^- oxidation to Cl_2 or HOCl in PEC systems is often evaluated in terms of faradaic efficiency (FE), which is the ratio of the measured HOCl/Cl_2 concentration to the theoretical one when passed through current. Hence, the sum of FE for HOCl and O_2 should ideally be unity (100%). The FE can be calculated based on the following formula (eqn (25)):

$$\mathrm{FE} = \frac{2 \times F \times n(\mathrm{Cl_2})}{Q} \times 100, \tag{25}$$

where F is the Faraday constant, $n(Cl_2)$ is the number of moles of Cl_2 produced, and Q is the number of charges passed through the electrochemical system.

5. Photocatalytic Cl_2/HOCl production

Photocatalytic systems are much simpler than their photoelectrocatalytic counterparts and can be more readily scaled up. One advantage of nanoparticulate powders used in photocatalytic systems is gram-scale preparation. Furthermore, the former does not need a specialized set up and can be used in a simple test tube or beaker in a slurry reactor without an external bias (or applied potential). Photocatalytic systems run with a single-compartment reactor where both oxidation and reduction occur in the same compartment, unlike PEC systems, which have dual compartments containing an anode and a cathode for both half-reactions. This, in turn, often requires the use of an electron scavenger, *e.g.* molecular O_2, to enhance the formation of Cl_2 because both oxidation and reduction take place on the same photocatalytic system. Photocatalytic materials can be prepared using various wet chemistry methods, such as sol–gel, hydrothermal/solvothermal and colloidal synthesis. These photocatalytic materials can be annealed further at high temperatures to improve crystallinity and enhance photocatalytic performance.

Metal oxides are commonly employed as photocatalysts owing to their chemical stability, suitable band gap, low toxicity, low-cost and facile preparation, as well as a highly positive valence band that is suitable for chloride oxidation reaction (COR). TiO_2, WO_3, Bi_2WO_6, and $BiVO_4$ are the most extensively studied metal oxide photocatalysts. WO_3 exhibits a moderate band gap (2.5–2.7 eV) and low toxicity and possesses suitable band edge positions for water and Cl^- oxidation (Fig. 2). It is well known that photoactivity depends on the size, morphology, and defect chemistry of photocatalysts. Lu *et al.* synthesized various WO_3 morphologies, including nanorods, nanowires, nanotube bundles, nanoplates and hollow microspheres, loaded with 1 wt% Pt as a co-catalyst and studied the structure-activity relationships in HOCl synthesis.[46] Pt/WO_3 hollow microspheres show the highest HOCl concentrations in 0.5 M NaCl and seawater at 14.52 μM (1.24 mg L^{-1}) and 4.34 μM (0.354 mg L^{-1}), respectively, with good stability up to four recycle tests. The author attributed the highest photoactivity to the hollow structure of WO_3 that facilitates charge separation. This work achieved the recommended free chlorine (0.2–2 mg L^{-1}) set by the WHO, highlighting its practical feasibility.

A systematic study on the effects of photocatalysts ($BiVO_4$, TiO_2, H_2WO_4, and Bi_2WO_6) and metal co-catalysts (Au, Ag, Cu, Rh, Pd and Pt) by Pang *et al.* disclosed that 1 wt% Pt/WO_3 exhibited the highest photoactivity with 17.6 μM HOCl produced in 1 hour while suppressing water oxidation (Fig. 4a).[10] A Pt co-catalyst enhances the catalytic activity by serving as an electron sink to capture photoexcited electrons from the conduction band (CB) of WO_3 and reduce O_2 to superoxide $O_2^{\bullet -}$ or H_2O. The same group also modified Pt/WO_3 by co-loading with various other metals as a co-catalyst. The Pt–M (M = Ni, Cr, Mn, Co, and Zn) co-catalyst improves the selectivity toward Cl^- oxidation to HOCl and promotes the decomposition of H_2O_2 (a product of ORR) to prevent its reaction with formed HOCl (Fig. 4b); Pt–Mn/WO_3 shows the highest HOCl production (37 μmol h^{-1}), which is twice that of Pt/WO_3 in an earlier work.[47] However, the dissolution of Mn presents a problem for recyclability and long-term usage of Pt–Mn/WO_3. Moreover, precise control must be taken to avoid the formation of MnO_x, which favours the oxidation of water over Cl^- oxidation.[48] Interestingly, the formation rate of HOCl is suppressed severely over Pt–M (M = Fe, Cu, and Ag). To ease recyclability in heterogeneous photocatalysis, a magnetic material, like Fe_3O_4, is typically incorporated into catalytic material designs for magnetic separation. Wang *et al.* constructed a multishell quaternary Pt/WO_3/SiO_2/Fe_3O_4 photocatalyst that achieved 6.31 μM HOCl in 2 hours.[49] The SiO_2 intermediate layer prevents an electron transfer from WO_3 to Fe_3O_4, inhibiting the loss of activity in HOCl generation.

A family of metal tungstate (MWO_4, where M is a bivalent metal) has emerged as a new type of photocatalyst owing to its low toxicity, low-cost and earth-abundant starting materials.[50] Wide band gap $ZnWO_4$ nanorods show a hypochlorite (OCl^-) yield of 1.01 μg mL^{-1} in seawater.[51] The production yield increases 2.5-fold when $ZnWO_4$ is loaded with an IrO_2 co-catalyst due to higher selectivity of Cl^- oxidation on IrO_2. More recently, Han *et al.* reported that $MnWO_4$ with a band gap of 2.83 eV could produce 12.6 μM h^{-1} HOCl in 0.5 M NaCl with

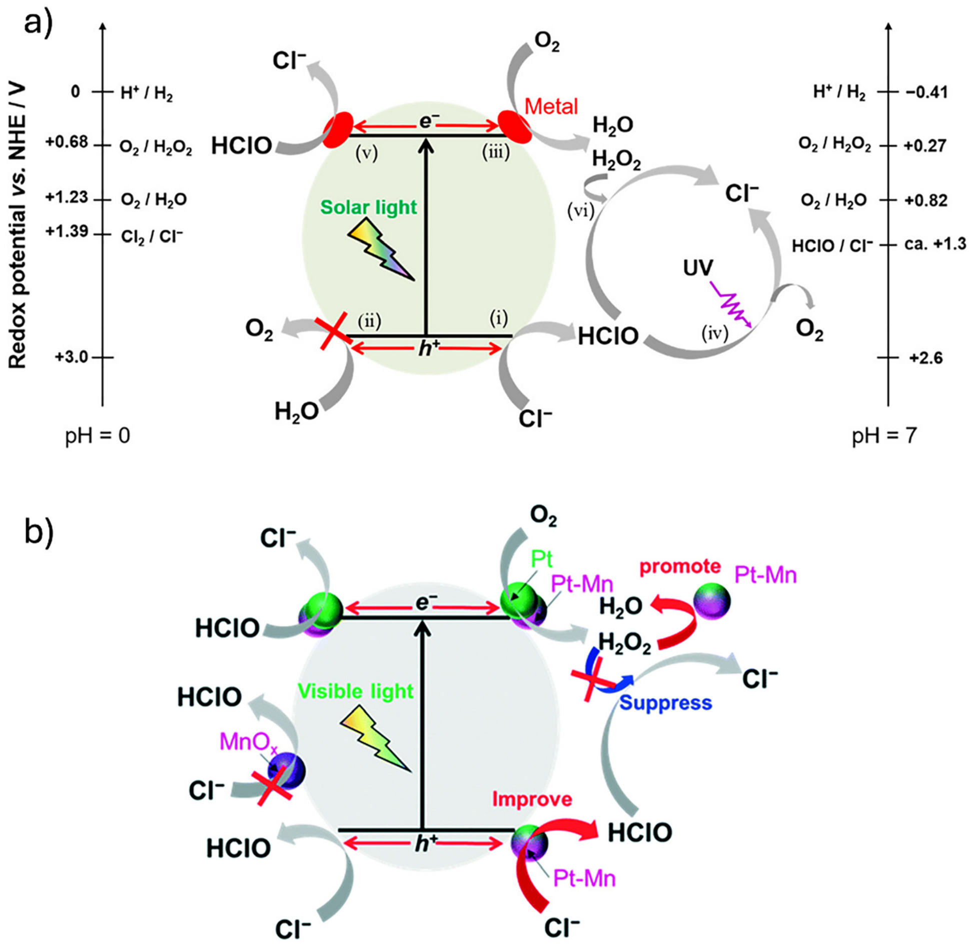

Fig. 4 Schematic of the Cl^- oxidation mechanism over (a) Pt/WO_3; reproduced from ref. 10. Copyright 2020, the American Chemical Society; and (b) $Pt-Mn/WO_3$ photocatalysts; reproduced from ref. 47. Copyright 2022, the Royal Society of Chemistry.

good stability and recyclability of up to four runs, paving the way toward promising noble metal-free photocatalysts.[52] In another work, the same group constructed a Z-scheme WO_3/CdS photocatalyst. An excited electron in the CB of CdS serves to reduce O_2 to $^{\bullet}O_{2-}$ and a photogenerated hole in the VB of WO_3 oxidises Cl^- to free Cl_2 (3.54 mg L^{-1}),[53] with a much higher activity than Pt/WO_3 (1.24 mg L^{-1} free Cl_2).[46] This work demonstrates the feasibility of designing promising noble metal-free photocatalysts for HOCl synthesis. Notably, noble metals, like Pt and Au, are not involved in Cl^- oxidation but are used to quench the excited electrons by capturing them from the VB of the photocatalyst. A similar quenching role can be applied through a Z-scheme mechanism or other types of photocatalyst design, thereby reducing the material cost in catalyst development.

In 2020, Li *et al.* investigated the origin of elevated Cl_2 in the atmosphere using KCl-coated TiO_2 to understand atmospheric Cl_2 chemistry in urban areas.[54] Although this work is not directly related to COR *via* seawater splitting, it shows a strong correlation between the amount of surface-bound Cl^- and the amount of Cl_2 evolved. TiO_2 is widely used in photocatalytic research due to its low cost, low toxicity and high chemical stability in a wide pH range.[55] Nonetheless, due to the fast charge carrier recombination and low photocatalytic activity, metal nanoparticles are often required to boost photoactivity. Okada *et al.* systematically studied the effects of pH on seawater splitting over Pt/TiO_2 (0.1 wt% Pt) and demonstrated a near stochiometric evolution of H_2 and Cl_2 with a minor O_2 evolution from direct water oxidation for over 14 hours (Fig. 5a and b); the selectivity toward Cl_2 formation is 81.1%, highlighting preferential oxidation of Cl^- over water oxidation.[32] High Cl_2 evolution was detected in an acidic (pH 1) seawater solution driven by the change in the VB maximum of TiO_2, contributing to stronger Cl^- oxidation at low pH. In another work, Jadwiszczak *et al.* found that PEC Cl_2/HOCl synthesis in acidic environments can suppress their decomposition to chlorates and oxygen, thus favouring acidic conditions for promoting high Cl_2/HOCl yields.[33] Nonetheless, the Cl_2 evolution could not be detected in neutral and basic conditions in Okada's work. The reason for inactivity is attributed to the rapid decomposition of HOCl to ClO_3^- and Cl^- ions. Additionally, the competing reactions between Cl^- and OH^- oxidation at high pH, which favours the latter, could be another reason for inactivity.[56,57] More recently, the same group studied the effects of Pt loading

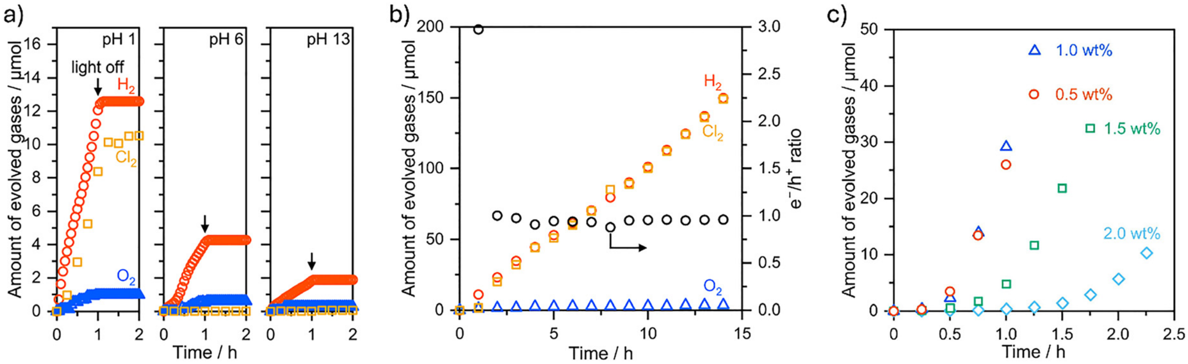

Fig. 5 Photocatalytic seawater splitting (0.5 M NaCl) over Pt/TiO_2 (a) at different pH values (1, 6, 13) and (b) time course reaction over 14 hours. Reproduced from ref. 32. Copyright 2024, the Royal Society of Chemistry. (c) Time course reaction with different Pt loadings (wt%) on TiO_2. Reproduced from ref. 58. Copyright 2025, Elsevier.

on the production rate of H_2 and Cl_2.[58] The rate of gas evolution increases as the Pt loading increases and reaches a maximum at 1.0 wt% (Fig. 5c). Beyond 1.0 wt% of Pt loading, the photoactivity decreases most likely due to the light-shading effects of Pt. Notably, it is worth noting that Pt dissolution in an acidic seawater solution is triggered by photoirradiation, with two plausible mechanisms of dissolution. First, photogenerated electrons reduce PtO_x to Pt, and PtO_x reacts with Cl^- to form $PtCl_6^{2-}$ species, which are soluble in an aqueous solution. In the second mechanism, photogenerated electrons and holes reduce PtO_x and oxidize Cl^- to Cl_2, respectively, where Cl_2 then reacts with Pt to form soluble $PtCl_6^{2-}$.

Rh/Cr_2O_3 and $RhCrO_x$ alloy are used extensively as a co-catalyst for the hydrogen evolution reaction (HER) in photocatalytic water splitting.[59–62] Importantly, CrO_x overlayers have been shown to act as a protective layer to prevent unwanted side reactions and undesirable species in water splitting.[63] Nonetheless, their use in seawater splitting is relatively unexplored; thus, the knowledge about their roles and performance in seawater splitting is limited. Okunaka *et al.* investigated the role of co-catalyst (RhO_x, CrO_x, and $RhCrO_x$) loaded on $SrTiO_3$:Al for HOCl production in aqueous NaCl solution.[64] It was found that only $RhCrO_x$ shows a significant HOCl production along with H_2 evolution, where the Rh species promotes H^+ reduction and CrO_x suppresses HOCl decomposition. Additionally, the role of $RhCrO_x$ is to enhance the charge separation between the co-catalyst and the photocatalyst.

The extraction and insertion of surface lattice atoms/ions *via* self-oxidation of lattice Cl^- in Cl-containing photocatalysts (*e.g.* AgCl and BiOCl) to Cl_2 by a photogenerated hole provide smooth oxidation, often followed by a structural change during a catalytic cycle. The lost/oxidized lattice Cl^- is then replaced by

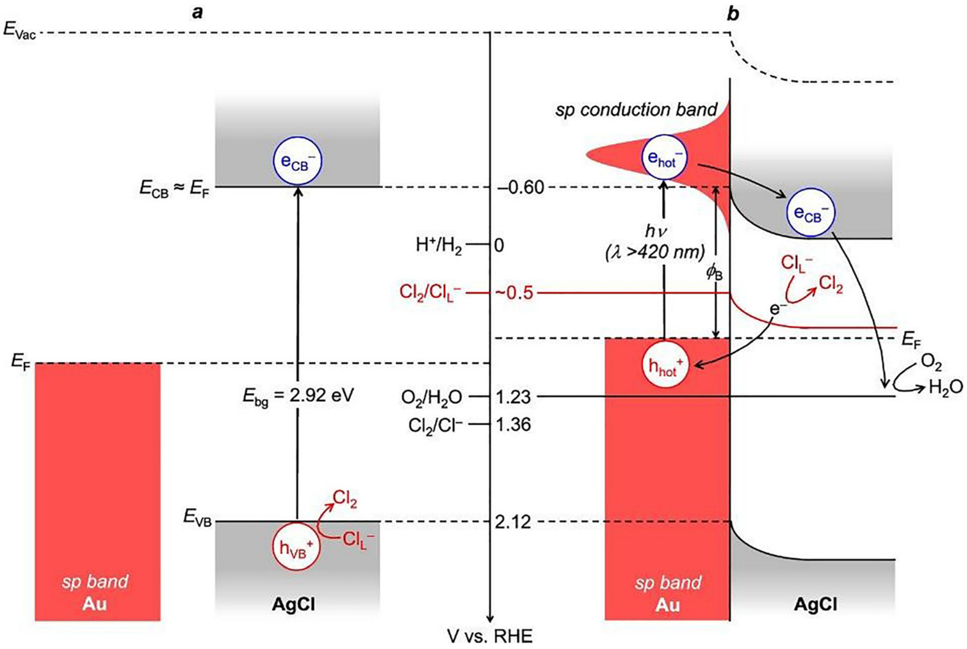

Fig. 6 Band energy diagrams of (a) AgCl and (b) Au/AgCl. Reproduced from ref. 66. Copyright 2023, the American Chemical Society.

Cl^- ions in the bulk seawater solution, creating a chlorine cycle. The participation of lattice atoms/ions as active species in chemical reactions is known as the Mars–van Krevelen (MvK) mechanism. Hirai's group reported that the compensation of Cl^- ions in seawater solution suppresses photocatalyst deactivation.[65] In light of this characteristic, AgCl and BiOCl have advantages for photocatalytic Cl^- oxidation in seawater splitting. Although wide band gap AgCl scarcely exhibits photocatalytic activity, loading Au NPs onto AgCl drastically boosts Cl^- oxidation with a HOCl formation yield of 21.4 μmol, as reported by Shiraishi *et al.*[66] The localised surface plasmon resonance (LSPR) in Au NPs enables visible light (>420 nm) absorption to create hot electrons (e_{hot}^-) and holes (h_{hot}^+), where the latter oxidises lattice Cl^- in AgCl to Cl_2 (Fig. 6). Although the redox potential of Cl^-/Cl_2 (1.36 V *vs.* RHE) is more positive than the VB of Au NP, the photogenerated holes in the VB of Au NP can oxidize the lattice Cl in AgCl, circumventing the insufficient redox potential. The oxidation of lattice Cl^- was confirmed by XPS analysis and control experiments.

Another promising photocatalyst that has garnered attention is the non-toxic, inexpensive, and wide band gap BiOCl (3.1–3.3 eV). The structure is made of $[Bi_2O_2]^{2+}$ slabs interleaved between double slabs of $[Cl]^-$ along the [001] direction, which creates an internal electric field (IEF) along the crystal orientation perpendicular to the $[Bi_2O_2]^{2+}$ and $[Cl]^-$ slabs that promote charge separation and migration (Fig. 7a–c).[52] Atoms in the $[Bi_2O_2]^{2+}$ layers are held by a covalent bond, while the interaction between the [Cl–Bi–O–Bi–Cl] stacks is held together by a non-covalent van der Waals force.[67] Therefore, the removal of Cl^- ions from the crystal structure of BiOCl is much easier owing to the weaker van der Waals interaction, which is beneficial for Cl^- lattice extraction and insertion, as demonstrated in chloride ion batteries,[68] which may have implications for photocatalytic Cl^- oxidation.

Wang *et al.* demonstrated that the insertion/extraction of Cl^- proceeded on the {110} facet, as evidenced by the photocorroded {110} facet of the BiOCl microplates after several catalytic runs (Fig. 8d and e).[56] The finding is reinforced by DFT calculations, which suggest that the open channel {110} facet exhibits lower overpotential and easier lattice Cl^- transport than the {001} facet, giving simultaneous advantages of Cl^- extraction and oxidation (Fig. 8f and g). In another work,

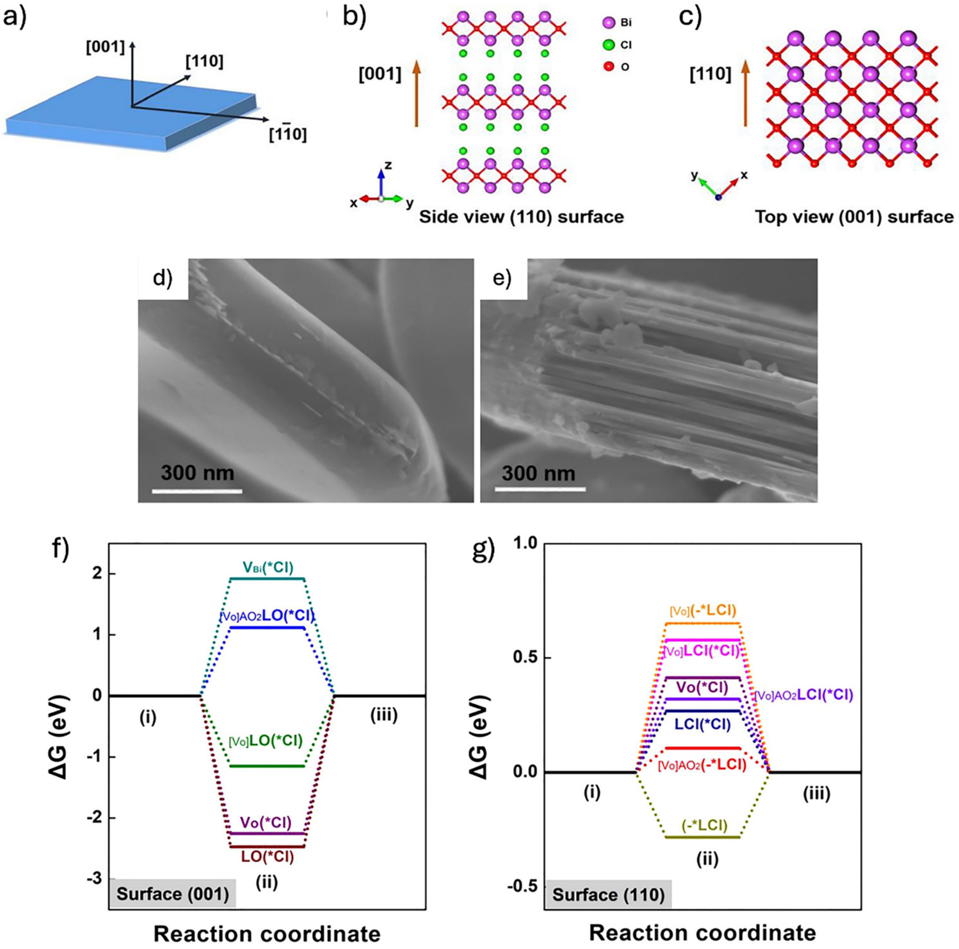

Fig. 7 Simplified surface of BiOCl with (a) different facets. (b) Side view of the surface along the [001] direction and (c) top view of the surface along the perpendicular [110] direction. TEM images of BiOCl (d) before reaction and (e) after reaction. DFT calculations of the free energy for the Cl_2 evolution reaction on the (f) (001) surface and (g) (110) surface. Reproduced from ref. 56. Copyright 2021, Elsevier.

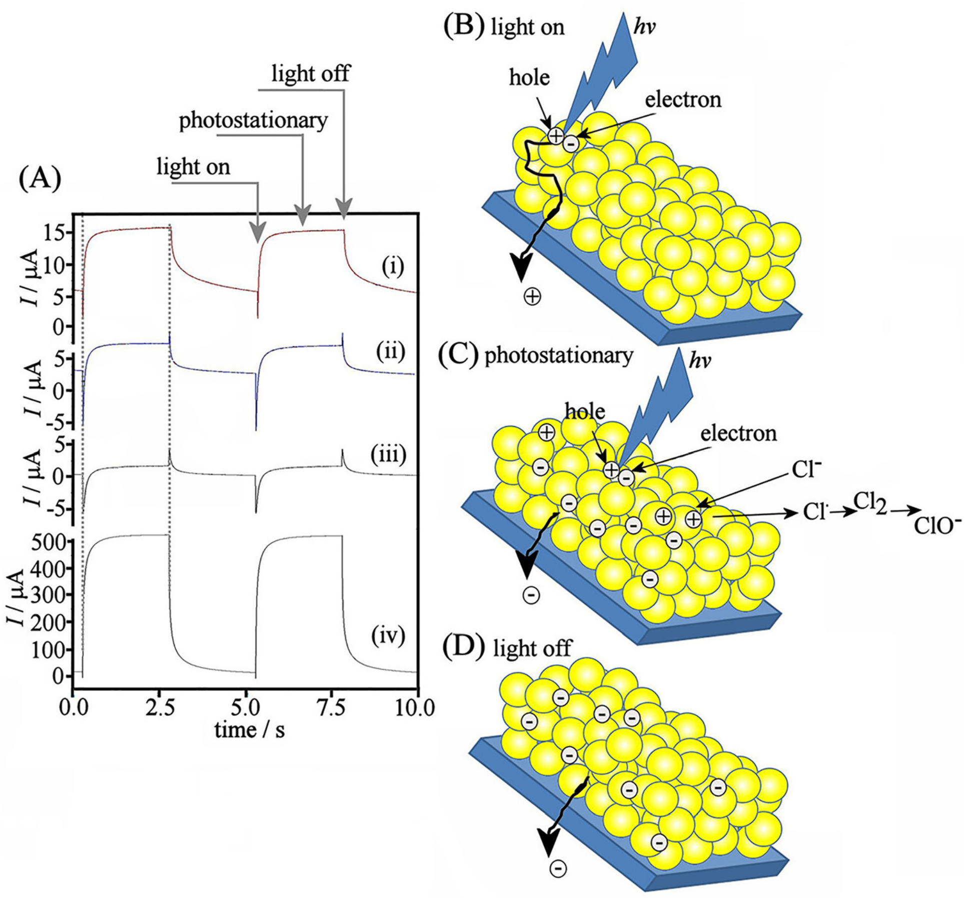

Fig. 8 (A) Transient photocurrent measurements for the as-deposited WO_3 electrodes at (i) 0.8 V, (ii) 0.5 V, and (iii) 0.2 V *vs.* SCE and (iv) annealed WO_3 electrode at 0.5 V *vs.* SCE. Illustration of charge behaviour (B) when irradiated with light, (C) under photostationary conditions, and (D) when light is off. Reproduced from ref. 79. Copyright 2013, the American Chemical Society.

Zhou *et al.* systematically investigated the effects of different facets {001} and {110}, on the formation rate and yield of HOCl. The highest production rate of RCS (95.9 μg L^{-1} min^{-1}) was achieved with the largest {001}/{110} ratio owing to the largest IEF, as verified by transient photocurrent response, EIS and PL spectroscopy; the lowest {100}/{110} ratio of BiOCl yields 75.6 μg L^{-1} min^{-1}.[36] The Cl^- lattice oxidation and extraction contribute to the weakening of Bi–Cl vibrations, the emergence of metallic Bi (reduction of Bi^{3+} to Bi^0), and the formation of oxygen vacancies, as confirmed by Raman spectroscopy, XRD and XPS.[36,69] The presence of molecular O_2 helps to prevent self-oxidation of lattice Bi^{3+} and regulate the electronic structure of BiOCl by adsorbing to the oxygen vacancies (V_0), usually leading to a higher photoactivity in Cl^- oxidation.

Doping foreign elements (non-metals or metals) into a host material has been a straightforward strategy for improving charge transport properties. In 2016, Li *et al.* doped Bi_3O_4Cl with carbon to boost the IEF by 126 times and achieved a bulk charge separation efficiency of 80% that enabled photocatalytic water oxidation without noble metals or electron scavengers.[70] Motivated by their work, Xu *et al.* reported that carbon-doped BiOCl (C-BiOCl) was found to enhance IEF and improve charge separation and migration as well as preference for Cl^- oxidation over water oxidation in photocatalytic Cl_2 formation.[71] A 2-fold enhancement in IEF in C-BiOCl leads to a 2-fold increase in the production rate of Cl_2 (0.23 mg L^{-1} min^{-1}) compared to that of pristine BiOCl (0.11 mg L^{-1} min^{-1}), underscoring a strong correlation between IEF and photoactivity. Nitrogen doping in BiOCl has the advantage of providing basic Lewis sites for reduction reactions. Shi *et al.* attempted the thermal decomposition of ammonium oxalate that delaminated bulk BiOCl into atomic-layer nanosheets and simultaneously introduced N dopants and O vacancies (N–O_V associate). The N–O_V associate reduces the exciton binding energy (from 199 to 46 meV) and lifetime (107.5 to 25.5 ms) to facilitate dissociation of an exciton into free charge carriers, leading to a HOCl production rate of up to 87.2 μmol g^{-1} h^{-1} (Table 2).[72]

The ocean absorbs around 30% of the CO_2 that is emitted to the atmosphere, which consequently decreases the pH of the ocean, also known as ocean acidification. The dissolution of CO_2 in water forms weak carbonic acid (H_2CO_3), which exists in equilibrium with (H^+) and bicarbonate (HCO_3^-) ions. A recent work revealed that dissolved CO_2 in a NaCl solution boosted the formation rate of Cl_2 on BiOCl by over 3-fold and 2-fold

Table 2 Summary of the photocatalytic performance of various photocatalysts in HOCl production

Photocatalyst	Light source	Reaction solution	[HOCl][a]/μM	Time /h	AQY (%)	Ref.
0.1% Pt/TiO_2	LED 365 nm	0.5 M NaCl (pH 1)	Cl_2: 10.3	1	~0.65% (365 nm)	32
1% Pt/TiO_2	LED 365 nm	0.5 M NaCl (pH 1)	Cl_2: 70 μmol h^{-1}	—	4.3% (365 nm)	58
1% Pt/WO_3	AM 1.5 G	0.5 M NaCl	17.6	1	2.3% (420 nm)	10
Pt–Mn/WO_3	300 W Xe (> 420 nm)	0.5 M NaCl	37	1	—	47
1% Pt/WO_3 hollow microsphere	Visible light	0.5 M NaCl	14.52	2	—	46
		Seawater	4.34	1	—	
Pt/WO_3/SiO_2/Fe_3O_4	White LED	0.5 M NaCl	6.31	2	—	49
$MnWO_4$	Visible light	0.5 M NaCl	12.6	1	SCC[b] 0.15%	52
IrO_2/$ZnWO_4$	UV 254 nm	Seawater	2.49 μg mL^{-1}	1	—	51
CdS/WO_3	LED (380–780 nm)	0.5 M NaCl	3.54 mg L^{-1}	2	—	53
0.1% $RhCrO_x$/$SrTiO_3$:Al	AM 1.5 G	1 M NaCl	~1 μmol	1	—	64
Au/AgCl	Xe lamp (> 420 nm)	0.55 M NaCl	21.4 μmol	24	SCC[b] ~0.03%	66
BiOCl	UV lamp	6 g L^{-1} NaCl	Cl_2: 0.125 mg L^{-1} min^{-1}	1	—	69
BiOCl	UV 254 nm	6 g L^{-1} NaCl	9.8 μmol	0.5	—	56
BiOCl	UV 254 nm	6 g L^{-1} NaCl	95.9 μg L^{-1} min^{-1}	—	—	36
C-BiOCl	UV 254 nm	6 g L^{-1} NaCl	0.023 mg L^{-1} min^{-1}	1	—	71
BiOCl–N–Ov	300 W Xe (> 400 nm)	0.5 M NaCl with CO_2 saturation	87.2 μmol g^{-1} h^{-1}	4	0.69% (400 nm)	72
BiOCl	UV lamp	0.51 M NaCl	19.8 μmol	0.5	—	73

[a] The default product measured was set to HOCl as determined using the DPD method. However, some studies reported the yield of Cl_2. [b] SCC refers to solar-to-chemical conversion.

compared to N_2-rich and O_2-rich atmospheres, respectively.[73] SEM images of BiOCl before and after photocatalysis disclose interlaminar deformation and distortion, which are probably caused by the insertion of CO_2 into the interlayers and anion exchange. The proposed mechanism of CO_2-mediated formation of Cl_2 in synthetic seawater is given by

$$HCO_3^- \rightarrow CO_3^{2-} + H^+ \tag{26}$$

$$CO_3^{2-} \rightarrow {}^{\bullet}CO_3^- + e^- \tag{27}$$

$${}^{\bullet}CO_3^- + H_2O + h^+ \rightarrow HCO_4^- + H^+ \tag{28}$$

$$HCO_4^- + 2Cl^- + 2H^+ \rightarrow HCO_3^- + Cl_2 + H_2O \tag{29}$$

6. Photoelectrochemical (PEC) Cl_2/HOCl production

In a photoelectrocatalytic system, HOCl formation occurs at the photoanode, and other reduction reactions proceed at the photocathode, including H_2 evolution, H_2O_2 production or CO_2 reduction (in the presence of CO_2). Advantages of photoelectrocatalysis are relatively simple electrode construction with tailored properties, such as controlled thickness, porosity, defects (or vacancies) and other surface properties. Photoelectrode performance is highly dependent on the interface, morphology and thickness of the thin film electrode. The thickness affects the light absorption (up to several μm), photocurrent generation and charge carrier diffusion length (up to several hundred nm). These properties are easily optimized to maximize photocurrent responses and charge transport efficiency. Moreover, it allows the use of various techniques, like layer-by-layer deposition, electrodeposition, pulse-laser deposition (PLD), and successive ionic layer adsorption and reaction (SILAR). Additionally, catalytic materials can be prepared using common methods, such as sol–gel and hydrothermal, and successively deposited on conducting substrates (ITO, FTO) by doctor-blading, drop-coating and spin-coating.

WO_3 exhibits high chemical stability in acidic solution (pH < 4), which is beneficial for photoelectrochemical Cl_2 synthesis (eqn (4)) but prone to dissolution in neutral or basic media.[60] An acidic seawater solution due to the presence of formed HOCl is advantageous for WO_3 because it ensures the WO_3 stability. At a higher pH, WO_3 forms WO_4^{2-} by reacting with OH^-, leading to its dissolution in alkaline media. As early as 1987, Desilvestro and Gratzel reported ~76% FE of Cl_2 production over polycrystalline WO_3 in 1 M HCl.[74] It has also been demonstrated that porous structures of WO_3 favour Cl^- oxidation over water oxidation. Recently, highly porous WO_3 nanosheets with a specific surface area of 100 m^2 g^{-1} and a thickness between 10 and 20 nm prepared by chemical bath deposition achieved 100% FE.[75] However, a rapid decrease in FE as the charge increased was observed most likely due to the formation of higher chlorine oxo species. Hill and Choi showed that WO_3 in PEC favoured the oxidation of Cl^- (with 95% consumption of photogenerated holes) and completely suppressed water oxidation to O_2 and peroxo species in aqueous NaCl solution.[76] A similar observation of suppression of water oxidation was reported by Mi *et al.* using a 0.1 M HCl aqueous solution.[77] These studies demonstrated WO_3 thin films as a promising photoanode for Cl_2 evolution.

Shi *et al.* reported a stable WO_3 film prepared by 25 cycles of deposition-annealing process that produced 1.95 mA cm^{-2} at 1.23 V (*vs.* RHE) in natural seawater. However, the FE of Cl_2 evolution was quite low (56%).[78] Thick, nanoporous WO_3 *ca.* 3 μm with particle size of 20–30 nm provides a large internal surface area that allows contact with electrolytes, achieving large saturation photocurrents of 4.5 mA cm^{-2} at 0.76 V (*vs.* Ag/AgCl), although the FE is moderate (70%) due to competing O_2 evolution.[33]

Annealing of thin films is usually performed to remove excess solvent, improve the crystallinity, control the structural phase, and create a strong interface contact between the sample and a substrate (ITO and FTO). A ''roll-on'' process was employed to deposit commercial nano-WO_3 on ITO. The annealed WO_3 film at 500 °C shows a much higher transient photocurrent and Cl_2 concentration due to enhanced interparticle charge transport by hopping between aggregates compared to the as-made WO_3 film (Fig. 8).[79] The influences of annealing temperature on the compositional phases and PEC performance of WO_3 electrodes were reported by Jo *et al.* At the annealing temperature of 500 °C, the WO_3 contained predominantly monoclinic (87%) and orthorhombic (13%) phases, which gave the highest photocurrent of 2.7 mA cm^{-2} and FE of 93% at 1.0 V (*vs.* Ag/AgCl).[80] The fraction of monoclinic increases as the annealing temperature increases, which induces more defects and increases donor density for enhanced PEC performance. However, too large a concentration of defects can be detrimental to the PEC performance of WO_3 in Cl^- oxidation because defects could serve as a recombination centre.[75]

Recently, Johnston and co-workers employed photoinduced absorption spectroscopy (PIAS) and transient photocurrent (TC) measurements to unravel the reaction order of Cl^- oxidation on a WO_3 photoanode.[18] It has been found that the rate of Cl_2 formation has a first-order dependence on the surface holes, $[h_s^+]$, albeit the faradaic efficiency is not unity (62%). The remaining 38% is speculated to be due to the formation of higher oxo species, such as ClO_4^- or Cl_2, trapped in the PEC cell, as no O_2 was detected in the study. Such a high selectivity of Cl^- oxidation over water oxidation reinforces the lower overpotential and higher exchange current density of the former reaction.[77,81]

Proton intercalation can modify the electronic structure and optical properties of WO_3, rendering H_xWO_3 a promising photocatalyst due to increased electron mobility and high conductivity.[82] Remarkably, Bartlett's group unravelled that fast electron injection from Cl^- ions into the VB of H_xWO_3 leads to 100% FE for Cl^- oxidation.[83] Such fast electron injection also suppresses oxidation of W^{5+} by holes, giving high photostability and stable photocurrent during Cl^- oxidation in 0.5 M NaCl at pH 4.

$BiVO_4$ has a moderate band gap (2.4–2.5 eV) and a deep valence band suitable for many oxidation reactions; therefore, it has been widely employed as a photoanode in water oxidation under visible light irradiation.[84,85] Nonetheless, the fast charge carrier recombination, low electron mobility, poor charge transfer and short hole diffusion length (~70 nm) become obstacles to achieving its theoretical maximum STH (9.2%) and current efficiency (7.5 mA cm^{-2}).[86] Doping $BiVO_4$ with other atoms or ions is a straightforward and efficient strategy that increases charge carrier density, improves charge separation and transfer efficiencies, introduces surface states, modifies the electronic band structure and enhances IPCE of $BiVO_4$.[87–89] Mo-doped $BiVO_4$ exhibits enhanced IPCE, charge accumulation and FE of 78% with ~7.5 μmol ClO^- produced at ~2.1 C compared to the undoped $BiVO_4$ owing to the increased donor density by Mo dopants in $BiVO_4$.[90] Similarly, Luo *et al.* reported that Mo-doped $BiVO_4$ showed a 6-fold increase in photocurrent and 42% IPCE in the wavelength range of 365–440 nm compared to pure $BiVO_4$ (10% IPCE).[91] The Mo^{6+} substitution of V^{5+} in $BiVO_4$ enhances electron donation and creates more carrier density, and further loading with the RhO_2 layer results in improved photostability in seawater.

The use of a multilayer strategy to improve charge separation and transport efficiency, as well as catalytic activity, is ubiquitous in designing efficient photoanodes.[86] In the construction of a multilayer photoanode, WO_3 is first deposited onto an FTO glass prior to $BiVO_4$ deposition, in which the WO_3 layer serves as an electron transport layer (ETL) and a hole mirror to block the transfer of holes to the FTO substrate, leading to an enhanced charge transfer. It was reported that a multilayer $BiVO_4/WO_3$ photoanode exhibited a low applied bias (0.5 V) to achieve high current efficiency (~80%) and HOCl concentration (660 μM) in the 2000 s under optimised conditions.[9] Without the WO_3 underlayer, the formation yield and current efficiency of HOCl are lower and require a much higher external bias. A similar $BiVO_4/WO_3$ photoanode has been extended to the PEC production of HOBr.[92]

Surface passivation with metal oxide overlayers has several benefits. The overlayer can serve as a protective layer to prevent photocorrosion or dissolution, as a co-catalyst to enhance activity and selectivity in Cl^- oxidation, as a hole (or electron) transport layer to boost charge transport, and as a passivating layer to quench surface states.[93] Okunaka *et al.* explored several metal oxides (MO_x; M = Mn, Co, Ni, Fe, Pt, and Rh) as a surface passivator on $BiVO_4/WO_3$ photoanodes to investigate the selectivity (O_2 evolution *vs.* HOCl production) of oxidation half-reaction.[48] All metal oxides except MnO_x favour the formation of HOCl owing to their lower overpotential for Cl^- oxidation (Fig. 9a). However, it should be noted that an accurate determination of each (O_2 and HOCl) overpotential in these photoanodes is difficult because both water and Cl^- oxidation occur with different selectivities.

A unique feature of monoclinic $BiVO_4$ is spatial charge separation by different crystallographic facets. $BiVO_4$ is known to accumulate photogenerated holes at the {110} facet for oxidation reactions and to direct photoexcited electrons to the {010} facet for reduction reactions.[76] Hence, selective deposition of cobalt borate (CoBi) as a co-catalyst on the $WO_3/BiVO_4$ {110} facets has been observed to enhance the charge transfer kinetics, photocurrent response and conversion of photogenerated holes to redox species at the anodic sites for improved Cl_2 production.[96]

A thin layer coating with amorphous cobalt oxide (CoO_x) prepared by pulsed laser deposition is demonstrated to act as a co-catalyst and to protect $BiVO_4$ against corrosion. The thickness of CoO_x overlayer from 2 to 5 nm is controlled using the number of laser pulses, with the optimum thickness of 3 nm achieving a current density of 2.5 mA cm^{-2} at 1.2 V (*vs.* Ag/AgCl) and 60% FE in 3 M KCl solution at pH 7 (Fig. 9b).[94] By studying various CoO_x precursor concentrations, Sayama's group achieved near 100% FE of HOCl formation with 0.01 M CoO_x precursor concentration (Fig. 9c).[95] Such an enhancement in FE

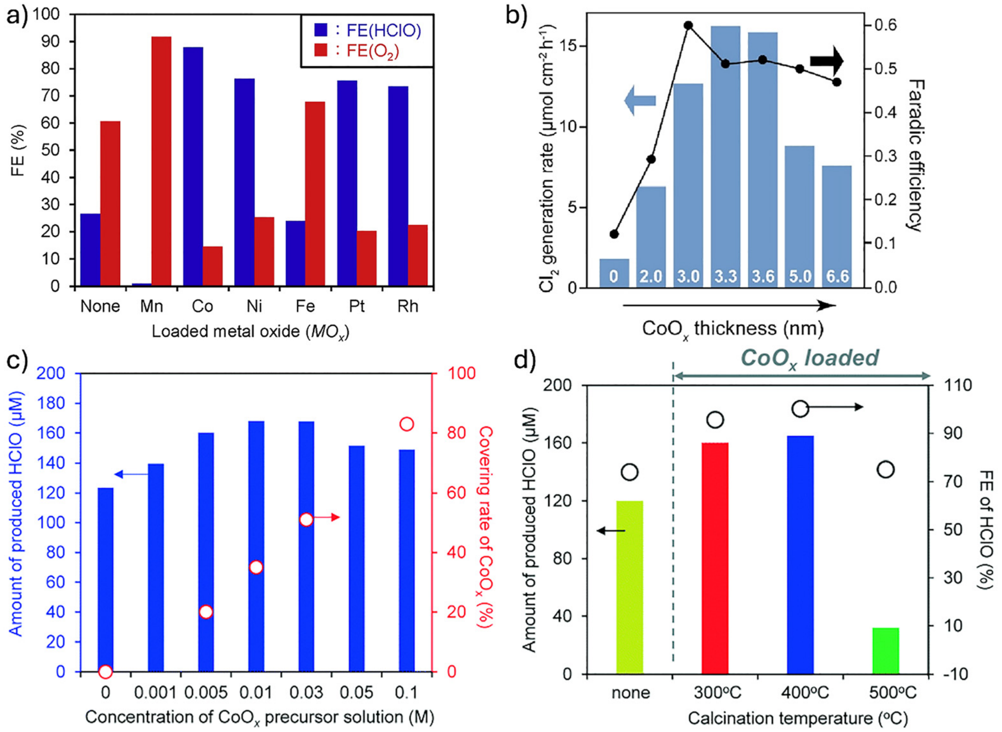

Fig. 9 (a) Faradaic efficiency of the HClO and O_2 formation on various metal oxide overlayers. Reproduced from ref. 48. Copyright 2020, Elsevier. (b) Cl_2 production rate and faradaic efficiency with different CoO_x thicknesses. Reproduced from ref. 94. Copyright 2023, the American Chemical Society. (c) HOCl concentrations with varying CoO_x precursor concentrations. (d) Effects of calcination temperature on the HOCl concentration and faradaic efficiency. Reproduced from ref. 95. Copyright 2021, the Royal Society of Chemistry.

is attributed to improved charge separation, efficient capture of photogenerated holes by CoO_x, and possibly the presence of active sites for Cl^- adsorption on CoO_x.[97] These studies showed that beyond a certain CoO_x thickness (>3 nm) and loading (>0.03 M), the FE and current density decrease due to increased charge carrier recombination, thus requiring optimisation studies to correlate to reach the right conclusion.

Sayama's work also showed that the calcination temperature of CoO_x precursor should be optimized at 400 °C because a higher temperature (>500 °C) promotes Co doping in $BiVO_4$, which may favour recombination of charge carriers, thus lowering the FE (Fig. 9d).[95] However, this finding seems to contradict Chauhan's work, which demonstrates that Co doping in $BiVO_4$ reduces the charge transfer resistance, facilitates charge carrier lifetime and improves the Cl^- oxidation kinetics.[98] The authors investigated the effect of Co dopant concentration in $BiVO_4$ and found that 0.05 mol% Co gives the highest photocurrent of 0.190 mA cm^{-2} at 1.1 V *vs.* RHE and 92% FE, which exhibited excellent stability against photocorrosion in acidic (pH 2.3) medium.[98] Other Co dopant concentrations yield much lower photocurrent and higher onset potential. The PEC performance is highly dependent on dopant concentrations; therefore, a systematic study of Co dopant concentration and its effect on the PEC performance must be optimized to achieve maximum FE and current density, as well as to resolve conflicting findings with other works.

The instability of $BiVO_4$ in electrolytes and acidic medium poses a problem for PEC reactions because it causes the dissolution of V^{5+} ions, leading to compositional and structural changes.[99,100] Chen and Wang theoretically demonstrated that $BiVO_4$ undergoes photocorrosion in an acidic medium (pH = 0) to form $BiCl_3$.[101] To prevent photocorrosion, a 20 nm-thick amorphous WO_3 layer is applied as a coating on $BiVO_4$ owing to its high chemical and electrochemical stability in acidic media and high selectivity for the COR over the WOR (Fig. 10a–c).[102] This strategy achieved a photocurrent density of 2.5 mA cm^{-2} at 1.42 V (*vs.* RHE) and FE of 85% (Fig. 10d). The photocurrent is remarkably stable for up to three hours.

Pristine TiO_2 suffers from fast charge carrier recombination and separation. Modification strategies, such as doping, defect creation, and structural transformation are often performed to improve charge separation and transfer. 1D TiO_2 nanostructures, such as nanorods and nanotubes, are favourable photocatalysts owing to their high specific surface area and improved charge transport properties. TiO_2 nanotubes demonstrate a higher FE of 60.6% at 0.2 V (*vs.* Ag/AgCl) than TiO_2 nanoparticles prepared by sol–gel for Cl_2 formation.[103] Ye *et al.* introduced oxygen vacancies (V_o) in TiO_2 nanotubes (TiO_2-V_o) and achieved 37.1 μmol h^{-1} cm^{-2} of Cl_2 with FE of 73.9%.[44] The improved PEC performance of oxygen-deficient TiO_2 nanotubes by 1.5-fold compared to bare TiO_2 nanotubes is attributed to the enhanced utilization of photogenerated charge carriers promoted by oxygen vacancies rather than selective COR over OER. Another study also showed an improved photocurrent in rutile TiO_2 with V_o and stability of Ti^{3+} surface states over 5 hours in PEC conditions.[57] It was suggested that Ti^{3+} sites

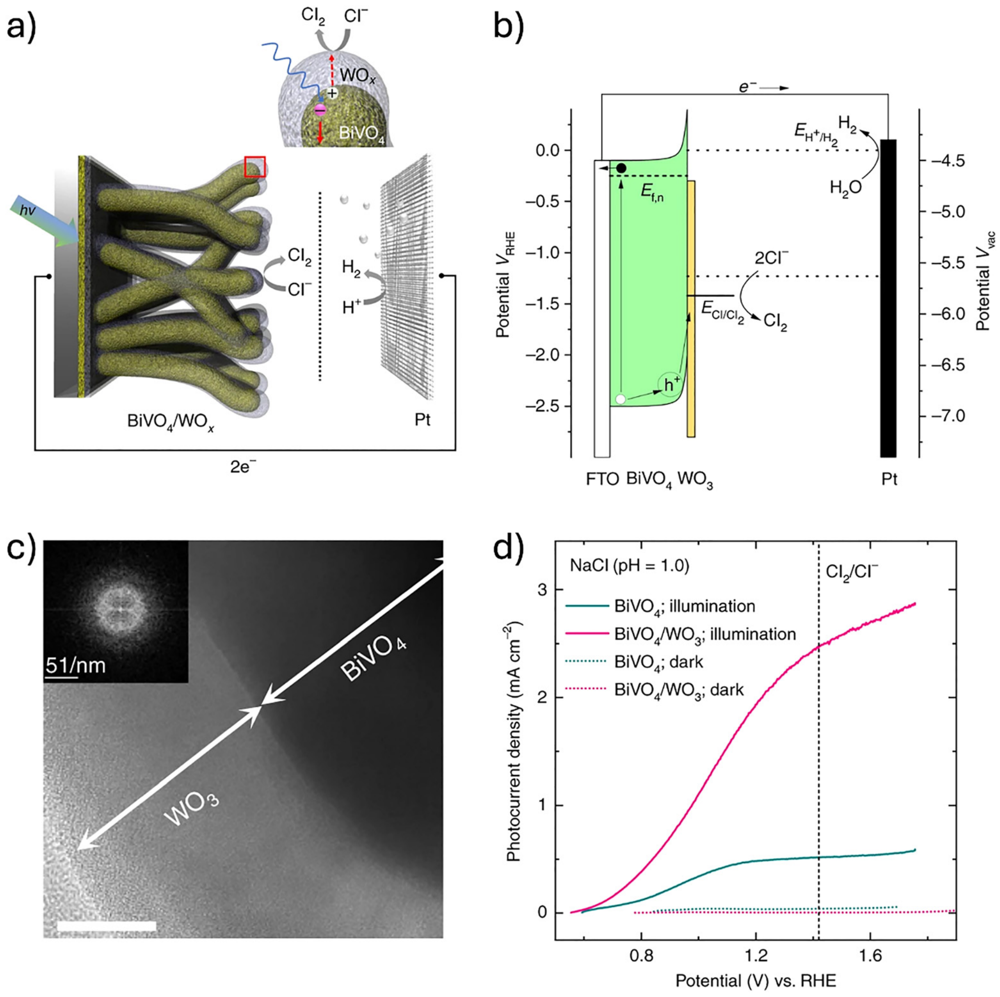

Fig. 10 (a) Illustration of the $BiVO_4/WO_3$ photoanode, (b) energy level diagram of the $BiVO_4/WO_3$ photoanode, (c) TEM image of $BiVO_4/WO_3$, and (d) photocurrent density across the applied potential. Reproduced from ref. 102. Copyright 2019, Springer Nature.

allow Cl^- ions to bind and react with photogenerated holes; however, no concrete spectroscopic evidence was provided in the study. Another study by Wu *et al.* combined DFT calculations and EPR trapping experiments to reveal that the activation of Cl^- on TiO_2-V_O occurs spontaneously (negative Gibbs free energy).[104] In summary, these findings highlight that oxygen vacancies (V_O) are highly beneficial for enhanced Cl^- adsorption and oxidation, leading to enhanced PEC performance in the Cl_2/HOCl formation (Table 3).[104,105]

7. Scalability challenges

PC and PEC seawater splitting demonstrates the feasible production of Cl_2/HOCl. Both the systems have merits and challenges in efficiently producing Cl_2/HOCl. The advantages, limitations and challenges of both the systems are summarised in Table 4.

Industrial and commercial practical applications require the high-performance, cost-effective, and long-term stability of photocatalytic materials (photocatalysts and photoelectrodes) and innovative large-scale reactor designs. These factors constitute scalability challenges for the large-scale production of Cl_2/HOCl. The efficiencies of photocatalytic materials are usually expressed using apparent quantum yield (AQY) and/or solar-to-chemical conversion (SCC). Many excellent photocatalysts with high AQY are wide-band gap semiconductors, such as TiO_2, WO_3, and BiOCl, which restrict the efficient utilization of visible light in the solar spectrum. Therefore, a search for other promising photocatalysts or modifications of wide-band gap photocatalysts is highly desirable.

The choice of photocatalytic materials is essential for achieving a high production rate and yield of Cl_2/HOCl. Single-component photocatalysts are often restricted by low photon absorption, fast charge carrier recombination and slow charge transfer, which contribute to low SCC and AQY in the visible light range. A typical and convenient method to improve charge carrier separation and transfer is to load a noble metal (Pt, Au, and Rh) co-catalyst onto a photocatalyst. Metal co-catalysts serve as an electron sink and a catalytic site for reduction reactions. This, however, places an additional material cost on the system. Many works have attempted to limit the usage of

Table 3 Summary of the photoelectrochemical performance of various photoanodes in HOCl production

Photoanode	[HOCl] or [Cl_2]	Photocurrent (mA cm^{-2})	Potential (V)	FE (%)	Ref.
WO_3	—	0.5–0.6	0.5–0.6[a]	76	74
WO_3	—	~0.8	1.6[b]	100	75
WO_3	—	3–3.5	0.9[b]	100	76
WO_3	140 μmol	1.95	1.23[c]	56	78
WO_3	—	4.5	0.76[b]	70	33
WO_3	—	2.7	1.0[b]	93	80
WO3	—	~0.62	1.0[b]	62	18
WO_3	—	~0.21	1.6[d]	30	81
WO_3	—	~0.60	1.23[c]	100	83
Mo:$BiVO_4$	—	~0.05	1.2[b]	78	90
RhO_2/Mo–$BiVO_4$	~1.25 μmol h^{-1}	2.16	1.0[c]	—	91
$BiVO_4/WO_3$	60 μM (500 s) 660 μM (2000 s)	~3.0	0.22[d] 0.50[d]	81 ~80	9
$CoO_x/BiVO_4/WO_3$	—	2	0.68[e]	88	48
$CoO_x/BiVO_4/WO_3$	12.5 μmol h^{-1} cm^{-2}	2.5	1.2[b]	~60	94
$CoO_x/BiVO_4/WO_3$	~160 μM	~2.3	1[c]	100	95
$CoB_i/BiVO_4/WO_3$	39.2 mg L^{-1}[f]	0.38	1.2[b]	—	96
Co:BiVO	—	0.19	1.1[c]	92	98
$WO_3/BiVO_4$	6 μmol	2.5	1.42[c]	85	102
TiO_2-NT	—	~0.5	0.2[b]	60.6	103
TiO_2-NT/Ti	37.1 μmol h^{-1} cm^{-2}	3.21	1.23[c]	73.2	44
TiO_2 (rutile)	—	8	1.0[a]	—	57
TiO_2-V_o	48.7 mg L^{-1} h^{-1}	~2.5	0.5[a]	—	104

[a] Referenced to SCE. [b] Referenced to Ag/AgCl. [c] Referenced to RHE. [d] Two-electrode cell system. [e] The steady current was set to 2 mA on a 1.5 × 5 cm^2 electrode and potential (*vs.* SHE). [f] At 2.3 V *vs.* Ag/AgCl.

such noble metal to below 1% wt. to achieve a compromise between high photocatalytic efficiency and material costs. Another promising strategy is to construct heterojunction photocatalysts, like Z-scheme or S-scheme, in photocatalysis to enhance carrier separation and transfer, as well as retain strong redox potentials for chloride oxidation.

The long-term stability of photocatalytic materials presents another challenge. The issues are corrosion in an acidic medium due to the presence of Cl_2/HOCl, and photocorrosion by charge carriers (electrons and holes) under light irradiation. Sayama's group demonstrated photocorrosion and dissolution of Pt co-catalysts, forming soluble $PtCl_6^{2-}$ when reacting with Cl^- in seawater. One simple strategy is to create a core–shell Pt-MOX (MOX = metal oxide) co-catalyst where a MOX shell protects the Pt core from photocorrosion and dissolution (Fig. 11a). A few stable and robust metal oxides have been commercially employed in the chlor-alkali process. Notably, TiO_2, RuO_2, and IrO_2 are widely used as coatings on anodes owing to their excellent chemical resistance in a wide range of pH. Forming this oxide coating can suppress the photocorrosion and dissolution of the metal core. For thin film photoanodes, such metal oxides can be deposited as a thin overlayer to protect the photoactive semiconductor (Fig. 11b). The direct deposition of an overlayer can be easily performed using photodeposition or electrodeposition, which creates robust thin films. For instance, Xiao *et al.* constructed hollow, mesoporous TiO_2 containing Pt/Cu_2O that maintained high photoactivity in seawater for 30 h.[106]

Reactor design is the most critical aspect of large-scale practical applications. When designing reactors, considerations include the reactor geometry, amount of light passing through the solution and reaching the photocatalyst, mass transfer process, leaching of photocatalysts from films or electrodes, accumulation of sodium salt, and separation and

Table 4 Comparison of key parameters in upscaling between PC and PEC seawater splitting

System	Photocatalysis (PC)	Photoelectrochemistry (PEC)
Efficiency	Produced Cl_2/HOCl concentration has already reached the benchmark value for water treatment set by WHO.[a] However, the AQY and SCC efficiencies are below 10% and 0.1%, respectively	Much higher Cl_2/HOCl concentration obtained than the benchmark value set by WHO, giving higher SCC efficiencies than PC The moderate operating potential (<1.2 *vs.* RHE) for most photoanodes is an advantage for higher efficiency
Selectivity	High selectivity of Cl_2/HOCl is usually obtained. In many works, minimal O_2 evolution from water oxidation has been observed due to its sluggish kinetics	Faradaic efficiency is usually high (>90%) for most metal oxide photoanodes, and the use of applied voltage is rather moderate
Scalability	Construction of large-scale PC panels or planar reactors is straightforward (without electrical wiring and connectivity) and cost-effective	Complex configuration, including external electrical bias integration of PEC cells, makes up-scaling difficult
	Photocatalyst films usually have lower SCC efficiencies than photocatalyst nanopowders	Photoelectrode thin films often exhibit non-uniformity for large electrodes, reducing the current density and efficiencies
	The leaching of immobilised photocatalysts from the films might be a problem	High Cl_2/HOCl concentrations obtained might be a merit for small-scale demonstration of water treatment using small portable devices
	Issues with oxygen flow input, mass transfer, and separation of oxidation (Cl_2/HOCl) and reduction (H_2) products	Product separation is readily available in two-compartment PEC cells
Cost	Construction of panels or planar reactors is relatively cost-effective	Complex configuration for large-scale PEC cells makes it less cost-effective than PC reactors
	Material cost is relatively high due to the use of noble metals (Pt, Au, and Rh) as a co-catalyst and electron sink	Material cost is low because many performing photoanodes are transition metal oxides
	The recovery of leached photocatalysts adds an extra cost	Electrical energy input is required to provide the applied potential

[a] The recommended Cl_2 concentration for water treatment is a maximum of 4 mg L^{-1} for drinking water, as recommended by US EPA, and 0.2–0.5 mg L^{-1} for residual disinfection of free chlorine, as recommended by WHO.

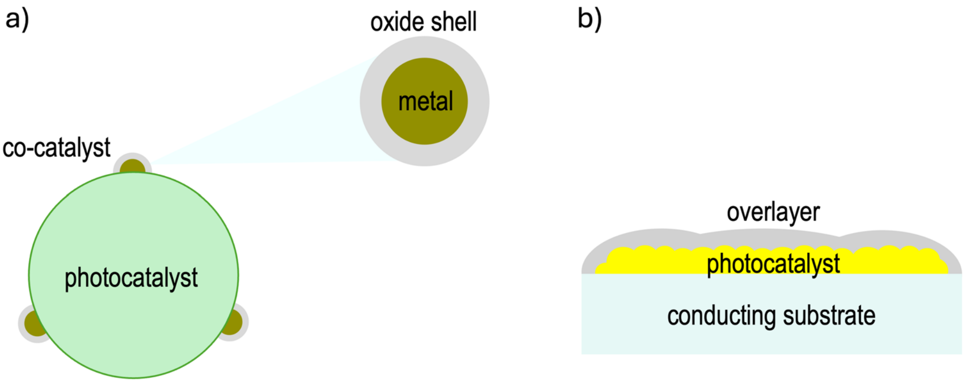

Fig. 11 Illustration of (a) oxide shell protecting the metal core and (b) overlayer protecting the photocatalyst from photocorrosion and dissolution.

collection of Cl_2/HOCl. Domen's group constructed a scalable panel reactor with 100 m^2 in size that consists of photocatalyst sheets (Fig. 12a).[107,108] The photocatalyst sheets were prepared by applying a spray method on frosted glass sheets. A similar design for photocatalytic seawater can be adopted, where seawater flows through the film panel and the gases evolved can be collected at the top. Because H_2 is the expected reduction product, there is a need for a dedicated separation of Cl_2 and H_2 gases. Fortunately, HOCl (resulting from the dissolution of Cl_2 in water) can be collected in a liquid phase, thereby easing the separation of H_2 and HOCl. Unlike pure water splitting, two further considerations must be taken into account, namely, the removal of accumulated sodium salt and oxygen flow input (where oxygen acts as an electron scavenger). The accumulated

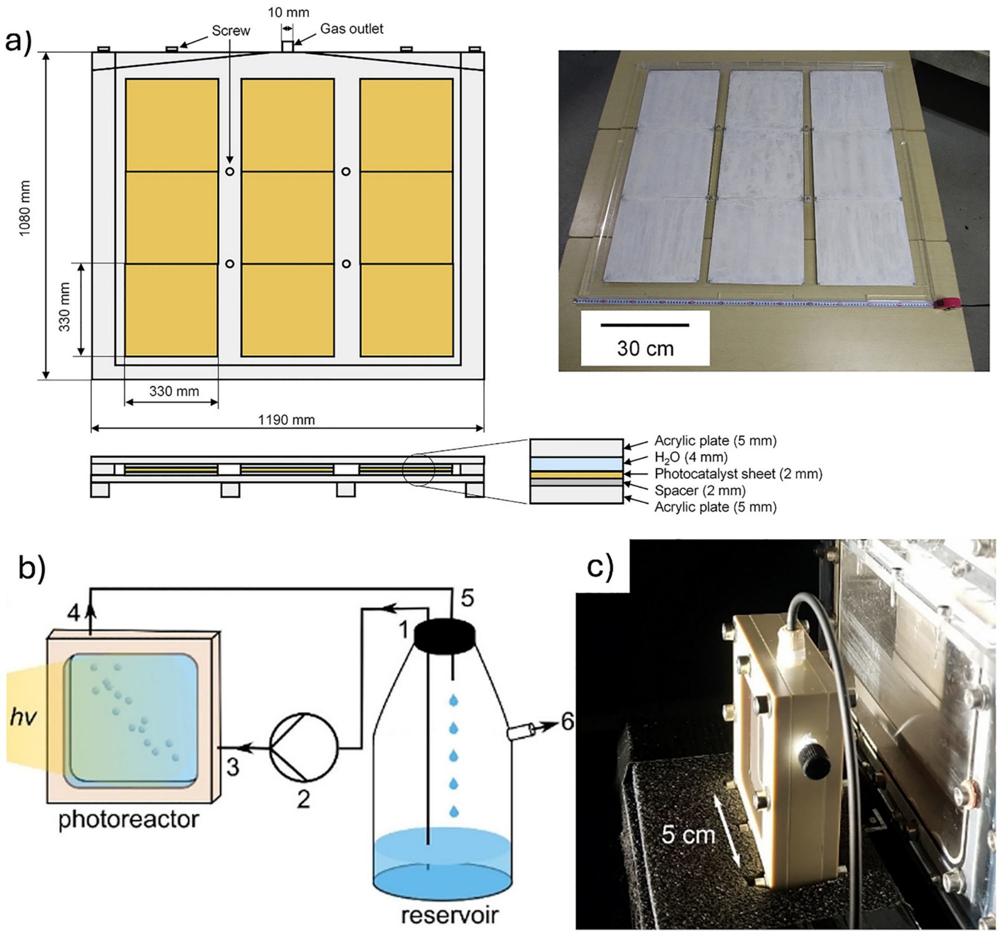

Fig. 12 (a) Scalable reactor design for a large-scale 100-m^2 panel reactor with 33 × 33 cm^2 films for photocatalytic water splitting. Reproduced from ref. 108. Copyright 2018, Cell Press. (b) Schematic diagram of large-scale panel experiments and (c) photograph of the 25 cm^2 photoreactor for the photoreforming of plastics, biomass and mixed waste. Reproduced from ref. 109. Copyright 2020, Wiley-VCH.

sodium salt on the film panel needs to be adsorbed, precipitated and filtered out for removal. Considering that the salinity of seawater is usually 3.5% (∼0.6 M) NaCl, which is relatively low compared to the one used in the industrial chlor-alkali process, precipitation of sodium salt is much less, and thus its removal is relatively easier. It should also be noted that the solution of aqueous NaCl is temperature dependent; therefore, the temperature of the seawater solution must be controlled to avoid salt precipitation during a photocatalytic reaction.

Another consideration is designing moderate-scale configurations for photocatalytic seawater splitting with a similar design to flow cells with a low-cost LED light source externally mounted to the cell. Uekert *et al.* designed a 25 cm^2 CN_x/Ni_2P panel for a real-world demonstration under low sunlight and seawater conditions (Fig. 12c and d).[109] The authors reported a loss of 50% efficiency in an upscaled (25 cm^2, 30 mL solution volume), custom-built flow reactor under real-world conditions. With this design, it is also possible to stack the cells into a larger configuration to boost the production rate and yield of Cl_2/HOCl. Considering that a tiny amount of Cl_2/HOCl (4 mg L^{-1}) is required for drinking water, this technology brings us a step closer toward real-world applications for on-site, on-demand production of Cl_2/HOCl for disinfection in remote areas.

Upscaling photochemical (PEC) reactors remains challenging because of several problems associated with PEC cells. However, PEC cells already have built-in compartments to collect H_2 and Cl_2/HOCl separately. The identified challenges for large-scale PEC cells include high cell efficiency (>10% STH), long life cycles and cost-effective fabrication process. Another issue is the incorporation of external bias to apply potential to the system. To overcome this issue, a research direction can be aimed at developing unassisted stand-alone PEC devices where one compartment carries out Cl^- oxidation using a photoanode and another carries out proton reduction using a photocathode. Large-sized photoelectrode fabrication presents another bottleneck that ensures homogeneous current density distribution. Dilger *et al.* successfully upscaled a PEC cell dimension from the typical 1 cm^2 to 40 cm^2 using $LaTiO_2N$ coated with co-catalysts.[110] The authors reported that the reduced activity and thus photocurrent density (by 54%) were attributed to the variation in the spatial distribution of potential and local photocurrent density. Overall, while fabricating homogeneous large-size photoelectrodes, controlling the optimised thickness of photoactive semiconductors and loading of co-catalysts, optimising cell geometry (including the distance of the light path), and inducing fast mass transfer dynamics remain challenging for upscaled PEC cells, notably when the electrode is larger than 10 cm by length, as remarked by Hankin *et al.*[111]

Very recently, Rodríguez-Gutiérrez designed a 3D-printed reactor and assembled ten such reactors to form a 100 cm^2 module for moderate upscaling with stable photocurrents for over 120 hours (Fig. 13).[112] This modular PEC reactor design paves the way for scalable outdoor applications. To minimize ohmic losses when photoelectrodes are in contact with an electrolyte, and to obtain efficient product separation in individual compartments, Tsampas's group constructed a zero-gap PEC device in which an anion exchange membrane (AEM) was sandwiched directly between a photoanode and a cathode.[113] The up-scaled device with an electrode area of 100 cm^2 preserves ∼98% of the photocurrent density exhibited by the 1 cm^2 photoanodes, demonstrating the practical feasibility and high performance of scalable PEC devices. More recently, a scalable PEC cell for H_2 and H_2O_2 production with a 144 cm^2 array panel has been reported.[114] Precipitation of electrolyte ($NaHCO_3$) on the photoanode films can be removed by rinsing with deionized water to recover the initial photocurrent. A similar design and post-treatment of photoanode films can be adopted for PEC chloride oxidation from seawater splitting; sodium salts can be removed by rinsing with water to recover the photoanode films.

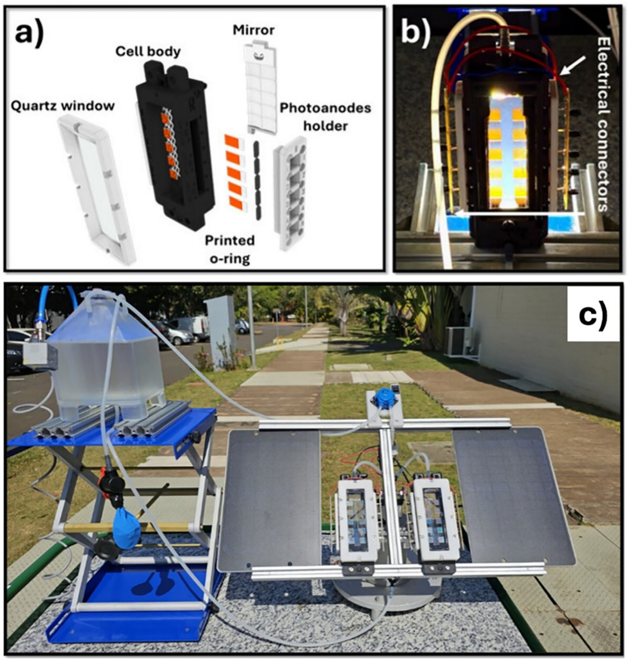

Fig. 13 (a) Illustration of the design of a modular PEC cell, (b) photograph of a real reactor with hematite photoanodes, and (c) outdoor demonstration for upscaled solar hydrogen production. Reproduced from ref. 112. Copyright 2025, the American Chemical Society.

8. Emerging photoactive semiconducting materials

Perovskite photocatalysts have garnered attention in water and seawater splitting. Metal halide perovskites (MHPs) adopt the crystal structure of ABX_3, where A and B are cations and X is a halide (Cl, Br, and I), with a well-known example of $CsPbBr_3$. The A site can also be occupied by organic cations, such as methylammonium and formamidinium in $MAPbI_3$ and $FAPbI_3$, respectively. MHPs are interesting and attractive because they exhibit high optical absorption coefficient, tunable optical properties *via* compositional engineering, defect-tolerant

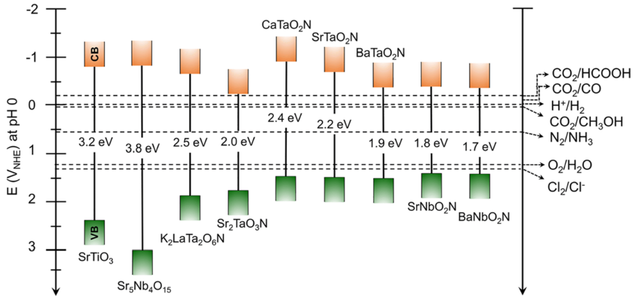

Fig. 14 Band gap and redox potentials of several perovskite oxynitrides. Reproduced from ref. 118. Copyright 2024, the Royal Society of Chemistry.

properties and large carrier diffusion lengths (~100 nm–~1 μm).[115] Due to the toxicity of Pb, several other metal cations have been explored, such as $CsSnI_3$, $CsGeI_3$, $Cs_3Bi_2I_9$ and $CsNaBiCl_6$. For perovskite oxides, piezoelectric properties present an advantage in applying mechanical vibration to enhance photoactivity. Although the work on Cl_2 /HOCl production from seawater splitting using MHPs has been insignificant, the potential for Cl_2 /HOCl production is desirable because the inherent Cl^- ions participate in the chlorine evolution reaction (CER) through the Mars–van Krevelen mechanism.

Perovskite-type oxynitrides $AB(N)_3$ (A = La, Ca, Sr, and Ba; B = Ti, Nb, and Ta) have recently emerged as promising photocatalysts due to their narrow band gap, which can harness visible light for photoredox processes (Fig. 14). $SrNbO_2N$ exhibits a narrow band gap (1.8–2.0 eV), a maximum current density of ~20.5 mA cm^{-2} and suitable band positions for seawater splitting. Trinh and Seo reported that porous $SrNbO_2N$/Nb photoanodes exhibited a photocurrent density of 2.6 mA cm^{-2} at 1.36 V_{RHE}, and three-fold selectivity for CER than OER.[116] The same group also reported that $Co(OH)_x$-loaded $BaTaO_2N$ promoted CER and subsequently decomposed Cl_2 back to O_2 and Cl^-, creating a self-sustaining steady-state Cl^- concentration in the bulk electrolyte.[117] This work paves the way towards sustainable H_2 production at the cathode without replenishing the NaCl electrolyte.

Perovskite oxides are another class of emerging photocatalytic materials with unique features, such as piezoelectric and ferroelectric properties. Moreover, perovskite oxides display superior stability to metal halide perovskites and perovskite-type oxynitride.[119,120] La_2NiO_4 achieves high activity for H_2 and Cl_2 evolution in coupled piezo-photocatalytic seawater splitting without any sacrificial agent.[121] Inducing mechanical vibration *via* ultrasonication improves the charge separation and transfer, which reduces the need for noble metal co-catalysts.[122] A self-generated $Na_{0.5}Bi_{0.5}TiO_3/Na_{0.5}Bi_{4.5}Ti_4O_{15}$ heterojunction also exhibits a decent photoactivity in seawater splitting albeit the HOCl concentration was not quantified.[123]

Porous coordination polymers, including metal–organic frameworks (MOFs) and covalent organic frameworks (COFs), are porous and crystalline materials with large surface areas, high porosity, diverse structures and topologies, and tunable electronic and optical properties through molecular engineering. These remarkable features render them promising in photocatalysis, electrocatalysis and photoelectrocatalysis. The catalytic activity and selectivity in MOFs are dictated by the unsaturated metal nodes and functional organic groups.[124] Moreover, the existence of charge transfer (linker-to-linker, metal-to-ligand, and ligand-to-metal) provides photoactive characteristics to MOFs.[125] Additionally, porous solid materials exhibiting different properties than the original MOFs can be prepared by pyrolysis of MOFs.

MOFs have been widely investigated for their promising applications in gas and liquid separation, membrane filtration and molecular sieving. The high-surface area and porosity offer a high capacity for ion adsorption, including chloride (Cl^-). Although the direct use of MOFs for the production of Cl_2/HOCl *via* seawater splitting is still limited and at an early stage of development, electrocatalytic and photocatalytic H_2 and O_2 evolution in seawater splitting have been demonstrated.[126,127] Jothi *et al.* demonstrated that bimetallic CuV-MOF showed significant CER activity albeit the faradaic efficiency was not quantified.[128] High durability and stability of several MOFs under harsh and corrosive conditions of seawater offer potential for the design of robust co-catalysts or electrocatalysts to produce Cl_2/HOCl. For example, crystalline-amorphous ferrocene-based Ni-BDC-aNiOOH MOFs exhibit superior durability with ~90% retention of current density for over 400 hours.[129]

Bao *et al.* recently reported the selectivity of Ni-BDC/NM88B(Fe) MOF-on-MOF heterojunction in seawater oxidation.[130] Although the intermediate in CER generally has a lower Gibbs free energy and a lesser number of intermediates at both Fe and Ni sites, the lower adsorption free energy of OH^- governs the selectivity, thereby favouring OER over CER. The formation of the NiFeOOH protective layer defends Ni-BDC/NM88B(Fe) against dissolution by Cl_2, leading to an excellent stability of 200 hours. Ligand defect engineering has proven to be a viable strategy for improving durability in seawater splitting. The electronic structure of NH_2-MIL-88B(Fe) has been modified by introducing ligand vacancies using acetic acid, resulting in the suppression of Cl^- corrosion.[131]

Few studies have applied porous coordination networks to PC and PEC seawater splitting. The major focus in seawater splitting is the H_2 evolution in the presence of a sacrificial agent, notably a hole scavenger.[132] For example, Li *et al.* employed Au-loaded thioether-functionalised COF in PC seawater splitting and observed no formation of Cl_2 because the presence of triethanolamine effectively scavenges photogenerated holes.[133] Attempts have been made to test PC seawater splitting using a variety of COFs without hole scavengers; however, little or no photoactivity was observed.[134] Crown ethers discontinuously conjugated polymers (DCPs) showed reduced photoactivity in a narrow range of NaCl concentrations (0–0.6 M) in synthetic seawater.[135] The finding implies that the presence of Na^+ and Cl^- ions negatively impacts the photocatalytic performance. The crown ether moiety adsorbs ions, leaving only the proton to interact with the active sites. In contrast, 2,4,6-trihydroxy-1,3,5-benzenetricarbaldehyde (TPBD) COF shows enhanced photoactivity in seawater due to the strong polorisation effect induced by C=O groups, leading to better charge separation and transfer.[136] Similarly, thieno[3,4-*c*]pyrrole-4,6-dione (TPD) COFs exhibit higher photoactivity in seawater owing to their increased hydrophilicity and enhanced charge carrier separation and transfer.[137]

The limited studies in photocatalytic seawater splitting particularly chloride oxidation using COFs originates from the low charge mobility and rapid charge carrier recombination that often requires a hole scavenger which precludes oxidation of chloride.[138] Additionally, certain organic functional groups in COFs readily adsorb ions, preventing Cl^- from reaching the actual active sites for CER. Future work should be directed to investigating and controlling the hydrophilicity/hydrophobicity, improving charge mobility and charge transfer, and creating selective active sites for Cl^- adsorption and oxidation.

9. PC and PEC applications of Cl_2 and HOCl

The advanced oxidation process (AOP) based on reactive chlorine species (RCS) provides a feasible strategy for the removal of organic contaminants and pollutants. HOCl undergoes photolysis under UV light irradiation to form highly reactive radical species, like $Cl^\bullet$, $^\bullet OH$, and $^\bullet OCl$, which are strong oxidants. In fact, as discussed below, RCS exerts a much more powerful and selective oxidising ability than reactive oxygen species (ROS) in some cases, leading to more efficient degradation performance. As a result, *in situ* generated oxidants from HOCl have been utilised to drive oxidative reactions, and organic pollutant degradation and removal. A well-established chlorination process has been employed for over 100 years in drinking water treatment, swimming pool disinfection and medical disinfection/sterilization, underscoring a profound and ubiquitous use of Cl_2/HOCl in bacteria deactivation and pollutant degradation. It is therefore imperative to discuss the relevant applications of Cl_2/HOCl in various chemical processes, considering the impacts of PC and PEC production of Cl_2/HOCl.

(a) Bacteria deactivation and inhibition

Chlorination is a well-established and effective means of disinfecting drinking water, swimming pools, and wastewater treatment. Bacterial deactivation is utterly important for marine antifouling, wastewater treatment and drinking water disinfection. Photocatalytic antibacterial properties are usually tested using Gram-negative bacteria, such as *Escherichia coli* (*E. coli*) and *Pseudoalteromonas*, and Gram-positive bacteria, such as *Staphylococcus aureus* (*S. aureus*) and *Bacillus* sp. *E. coli* is a common Gram-negative bacterium found in contaminated water sources (lakes, rivers, and reservoirs) and food that can be pathogenic and cause poisoning, stomach pains and cramps, watery diarrhea, vomiting and fever. Thus, *E. coli* is commonly used as a model bacterium for bacterial deactivation.

Koo *et al.* showed the complete deactivation of *E. coli* in four hours over WO_3 photoanodes due to the *in situ* generation of HOCl as an active species.[30] In another work by Juodkazyte *et al.*, the complete deactivation of *E. coli* and *Bacillus* sp. was demonstrated using a WO_3 photoanode and was ascribed to chlorine radicals ($Cl^\bullet$ and $Cl_2^{\bullet -}$).[81] It is worth noting that $^\bullet OH$ radicals are less effective in bacteria deactivation compared to RCS, highlighting the superiority of the latter. For example, Sun *et al.* disclosed that $IrO_2/ZnWO_4$ displayed a higher sterilisation efficiency against *E. coli.* owing to a higher production yield of RCS (HOCl, ClO^-) than $ZnWO_4$, which generated mainly $^\bullet OH$.[51] Moreover, the quenching experiment verified that scavenging of $^\bullet OH$ led to a slight decrease in sterilisation efficiency, suggesting a minor role of $^\bullet OH$ compared to RCS. More recently, carbon-doped BiOCl (C-BiOCl) displays impressive *E. coli* deactivation in 40 minutes (Fig. 15).[71]

A quaternary $Pt/Fe_3O_4@SiO_2@WO_3$ photocatalyst shows good antibacterial effects on a broad spectrum of bacteria, including *E. coli*, *Pseudoalteromonas*, *S. aureus*, and *Bacillus*, with antibacterial rates of 90%, 83%, 86%, and 88%, respectively, in three hours.[49] When the same photocatalyst was applied for algae inhibition on *Dicrateria inornata* and *Chlorella* under visible light irradiation for 12 hours, the inhibition rates reached 93% and 95%, respectively. Lu *et al.* reported an impressive bacterial deactivation (>97%) in two hours and algae inactivation (>90%) in 8 hours using Pt/WO_3 hollow microspheres owing to high *in situ* generated free chlorine (1.24 mg L^{-1}).[46] More recently, a Z-scheme WO_3/CdS photocatalyst exhibits higher deactivation efficiencies (>94%) on *E. coli*, *Pseudoalteromonas*, *S. aureus*, and *Bacillus* in three hours.[53] The inhibition rate of *Dicrateria inornata* and *Chlorella* achieved >90% in 12 hours.

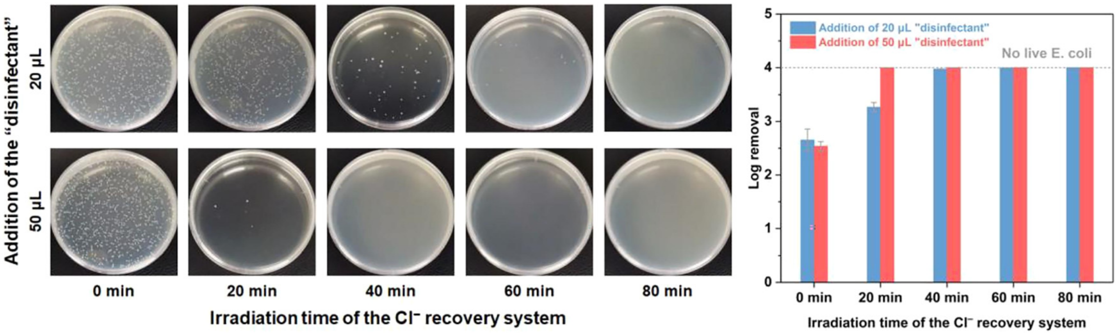

Fig. 15 Inactivation of *E. coli* over C-BiOCl with two different RCS concentrations. Reproduced from ref. 71. Copyright 2024, Elsevier.

In conclusion, these works demonstrate the practical feasibility of using *in situ* generated RCS for bacteria deactivation and algae inhibition. A potential future direction is to design portable photoreactors for PC or PEC systems that are suitable for use in remote areas for on-site sanitization and water treatments for small water sources or storage facilities, like wells, ponds and tanks. A small amount of RCS from PC or PEC seawater splitting is beneficial for sanitizing surfaces in the kitchen and lounge in rural houses.

(b) Ammonia removal

Ammonia is a key fertilizer for plant growth and nutrition in agriculture because it supplies nitrogen to improve crop quality. Although it is crucial for agriculture, excess ammonia in soil has negative impacts on human health and the environment, behaving as a pollutant in the atmosphere that causes acid rains, depositing in the soil and being dissolved in water (lakes, rivers), and changing species composition through soil acidification and direct toxic damage. Indirect discharge into wastewater containing ammonia nitrogen (NH_4^+–N) remains a challenging issue in agriculture and thus becomes a problem of environmental concern. Chlorine disinfectants have been used to remove NH_4^+–N by converting it to N_2. Utilizing photocatalytic Cl_2/HOCl production may eliminate the need for external chlorine sources. For example, Xiao *et al.* showed that RCS (Cl_2/HOCl) plays a critical role in NH_4^+–N degradation on TiO_2 nanotube photoanodes, where the degradation rates increase with NaCl concentration across a wide pH range.[139] Zhu's group demonstrated the practical feasibility of NH_4^+–N removal using landfill leachate and real wastewater as examples.[36,71]

The overall reaction for NH_4^+–N degradation proceeds according to eqn (30). The mechanism of NH_4^+–N degradation over a $BiVO_4/WO_3$ photoanode has been proposed to proceed *via* chloramine intermediates (NH_2Cl and $NHCl_2$).[140] COR produces $Cl^\bullet$, which abstracts H from NH_4^+ to form $NH_2^\bullet$; this radical reacts with HOCl to yield NH_2Cl (eqn (31)–(33)). A further reaction leads to an $NHCl_2$ and eventually N_2 evolution as described below (eqn (34)–(36)). NH_4^+–N can also be oxidized to NO_2^-–N and NO_3^-–N species (eqn (37) and (38)), thereby presenting competitive steps for selective N_2 formation in NH_4^+–N degradation.[141] The formation of NO_3^- is proposed to include reactive oxygen species (ROS), such as $^\bullet OH$, $O_2^{\bullet -}$, and H_2O_2.[142] Therefore, it is expected that COR in seawater solution would favour the selective formation of N_2 in the degradation of NH_4^+–N.

$$2NH_4^+ + 3HOCl \rightarrow N_2 + 3HCl + 3H_2O \tag{30}$$

$$Cl^- + h^+ \rightarrow Cl^\bullet \tag{31}$$

$$NH_4^+ + Cl^\bullet \rightarrow NH_2^\bullet + 2H^+ + Cl^- \tag{32}$$

$$NH_2^\bullet + HOCl \rightarrow NH_2Cl + OH^\bullet \tag{33}$$

$$NH_2Cl + Cl^\bullet \rightarrow NHCl^\bullet + H^+ + Cl^- \tag{34}$$

$$NHCl^\bullet + HOCl \rightarrow NHCl_2 + OH^\bullet \tag{35}$$

$$NHCl_2 + NH_2Cl \rightarrow N_2 + 3H^+ + 3Cl^- \tag{36}$$

$$NH_2^\bullet + OH^\bullet \rightarrow NH_2OH \tag{37}$$

$$NH_2OH + OH^\bullet \rightarrow NO_2^- \rightarrow NO_3^- \tag{38}$$

$$2NH_4^+ + 2ClO^\bullet \rightarrow N_2 + 4H^+ + 2Cl^- + 2H_2O \tag{39}$$

An early work by Ji *et al.* using a WO_3 photoanode disclosed that the complete degradation of NH_4^+–N to a major N_2 and minor NO_3^- occurred in 90 min and followed the pseudo first-order kinetics.[143] However, the degradation of NH_4^+–N over BiOCl was shown to follow the zeroth-order kinetics with almost complete degradation and 97% selectivity toward N_2 over BiOCl in 80 minutes.[69] Zhu's group reported that BiOCl with dominant {001} facets exhibited the degradation efficiency of 91.9% with stoichiometric Cl^- (in NH_4Cl) ions and near unity with extra Cl^- (from NaCl) in the reaction solution within 150 minutes.[36] Without Cl^- in the reaction solution, only 25.9% degradation was observed, highlighting the crucial role of RCS (Cl_2, HOCl, and $Cl^\bullet$) for promoting NH_4^+–N degradation. The higher degradation efficiency with increasing Cl^- content is attributed to the higher amount of RCS formed. Using a landfill leachate from a landfill in Zhongshan City as a real wastewater for treatment, the authors showed a degradation efficiency of 85.4% in 30 hours and 95.6% in 40 hours of treatment over BiOCl and C-BiOCl, respectively.[36,71] Nonetheless, Zhu and co-workers realised that the degradation efficiency under the Xe lamp is far inferior to that of the UV lamp.[71] The cause might be attributed to the less efficient photolysis of HOCl that creates radicals under the Xe lamp compared to that of the UV lamp.

Yan *et al.* disclosed that $OCl^\bullet$ radicals are responsible for achieving the complete degradation of NH_4^+-N in 120 min and boosting 100% selectivity towards N_2 in acidic NaCl solution (pH ≤ 6), as shown in Fig. 16a and b.[144] By scavenging and ESR trapping experiments, the authors disclosed that $OCl^\bullet$ radicals resulted from photolysis of HOCl under UV irradiation; the mechanism NH_4^+–N degradation is illustrated in Fig. 16c. Importantly, other works have also attributed the active species for NH_4^+–N degradation to $ClO^\bullet$ radicals.[141,145] It is worth noting that $^\bullet OH$ radicals are relatively inert to NH_4^+–N and thus are less effective in the degradation process. Similarly, the imperative role of RCS (Cl_2, HOCl, $Cl^\bullet$, and $ClO^\bullet$) in promoting the degradation of NH_4^+-N was reinforced by Zhang *et al.* using a $CoB_i/BiVO_4/WO_3$ photoanode, whereas $^\bullet OH$ radicals play a negligible role.[96] Notably, it has been revealed that $^\bullet OH$ reacts with HOCl to form $^\bullet OCl$ (and H_2O), showing an indirect participation of $^\bullet OH$ to form $OCl^\bullet$ active species.[104] Although $OCl^\bullet$ radicals are regarded as the primary active species in NH_4^+–N degradation,[146] HOCl plays a role in completing the cyclic chlorine species between Cl^- and $Cl^\bullet$ (or Cl_2), indicating complex reaction pathways (refer to eqn (29)–(37), and Scheme 1).

In summary, these reports show that RCS resulting from COR plays a predominant and significant role in degrading NH_4^+–N through chloramine intermediates and radicals, which

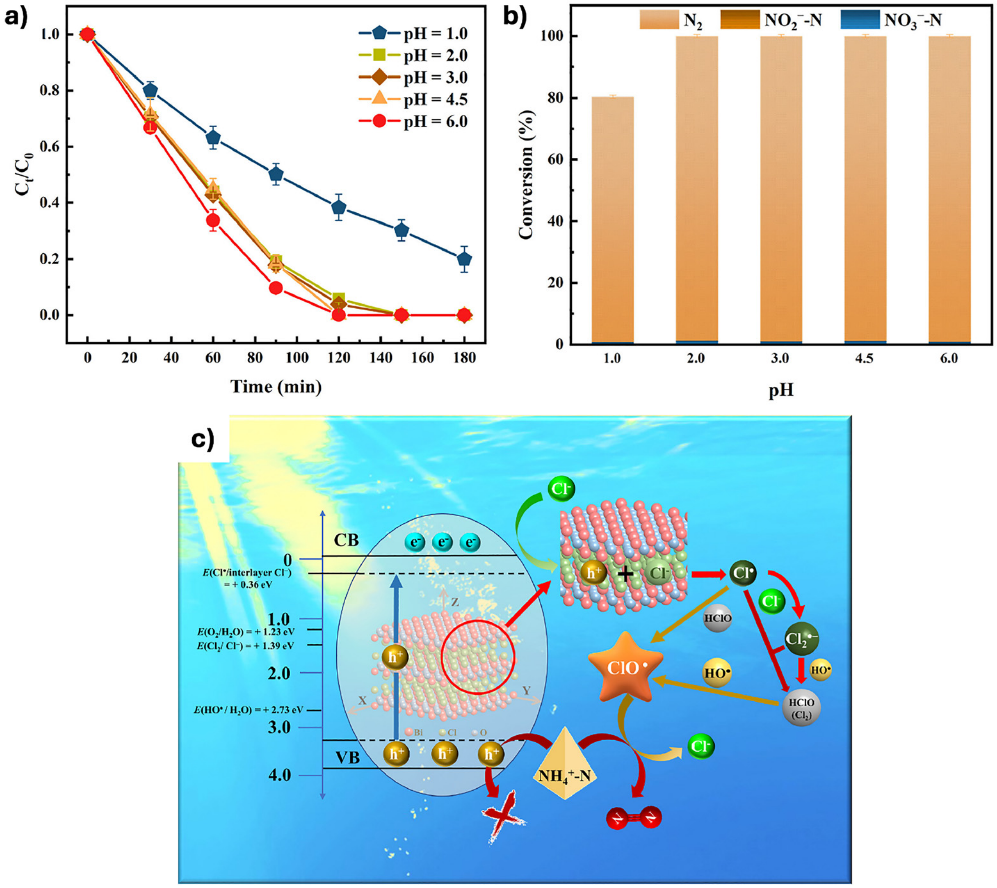

Fig. 16 (a) Time-course degradation of NH_4^+–N, (b) conversion of NH_4^+–N to different oxidised species (N_2, NO_2^-–N, and NO_3^-–N), and (c) a proposed mechanism of NH_4^+–N degradation in acidic water over BiOCl. Reproduced from ref. 144. Copyright 2021, Elsevier.

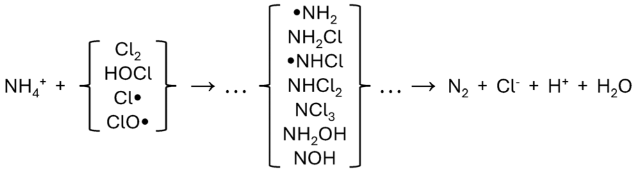

$$NH_4^+ + \left\{\begin{matrix} Cl_2 \\ HOCl \\ Cl\bullet \\ ClO\bullet \end{matrix}\right\} \rightarrow \ldots \left\{\begin{matrix} \bullet NH_2 \\ NH_2Cl \\ \bullet NHCl \\ NHCl_2 \\ NCl_3 \\ NH_2OH \\ NOH \end{matrix}\right\} \ldots \rightarrow N_2 + Cl^- + H^+ + H_2O$$

Scheme 1 NH_4^+–N degradation pathways to N2 through chloramine intermediates and radicals. Reproduced from ref. 96. Copyright 2023, Elsevier.

are much more efficient than reactive oxygen species (ROS). Despite a lower oxidation potential of $Cl^•$ (2.47 V *vs.* NHE) than $^•OH$ (2.80 V *vs.* NHE), $Cl^•$ is more selective and reacts faster with electron-rich moieties, such as NH_4^+.[143,147] The high selectivity towards N_2 formation renders PC and PEC degradation of NH_4^+–N using *in situ* generated RCS appealing, green and sustainable.

(c) Conversion of alkenes and alcohols

Due to the strong oxidising ability of HOCl in bacterial deactivation and pollutant degradation in wastewater, several works have extended its utility in the oxidation of alkenes and alcohols using *in situ* generated HOCl. HOCl behaves as a redox mediator and strong oxidant to oxidize organic compounds with a lower applied potential than the direct oxidation of such organic compounds by adding molecular O_2, H_2O_2 or *t*-BuOOH. For example, Yang *et al.* reported almost complete conversion and selectivity in the epoxidation of water-soluble alkenes on a $Co_2(OH)_3Cl/BiVO_4$ photoanode (Fig. 17a and b).[13] The mechanism of such epoxidation involves the formation of a secondary alcohol and terminal alkyl chloride as intermediates resulting from the reaction between *in situ* generated HOCl and alkenes (Fig. 17c). Such high photoactivity in epoxidation can potentially replace the use of *meta*-chloroperbenzoic acid (*m*-CPBA), which possesses a high risk of explosion and limits its large-scale utilization in alkene epoxidation.[148]

Oxidation of ethanol was demonstrated by *in situ* PEC HOCl generation on H_xWO_3, without the addition of external oxidants. Ethanol oxidation to acetaldehyde and acetic acid was mediated by HOCl serving as a strong oxidant – most likely through $^•OH$ and $Cl^•$ from the photolysis of HOCl – rather than direct oxidation on the H_xWO_3 electrode as confirmed by linear sweep voltammetry (LSV).[149] The EtOH conversion achieves 62% in 8 hours with 50% and 40% selectivity to acetaldehyde and acetic acid, respectively. The proposed reaction pathways are described by eqn (40)–(42). Such oxidation can be extended

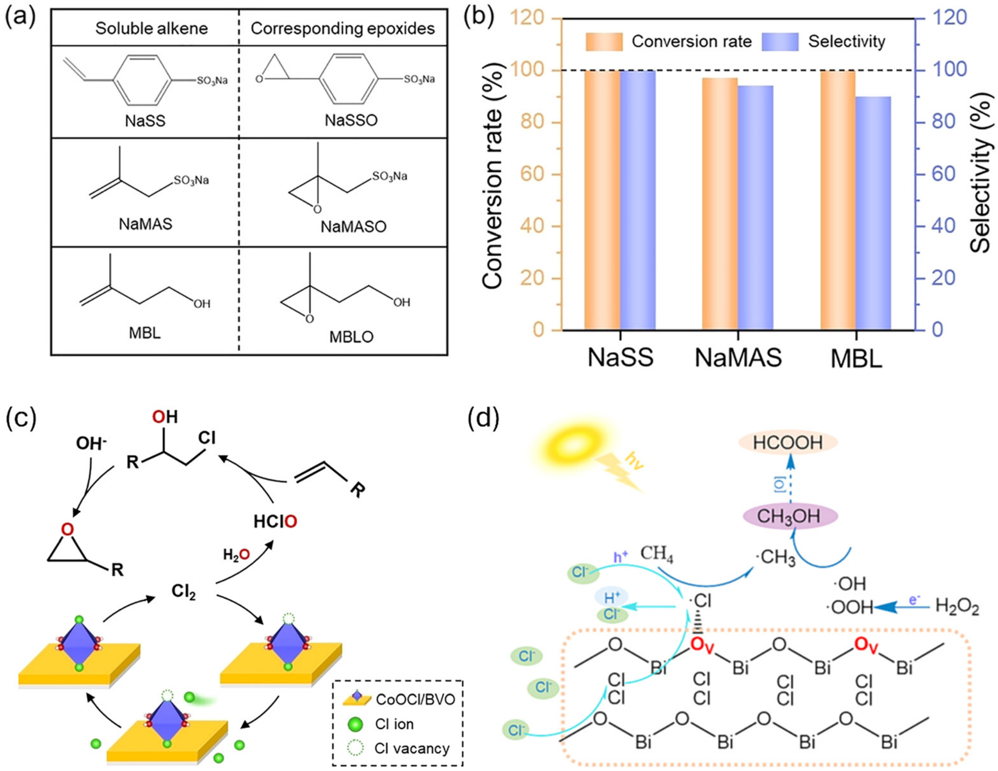

Fig. 17 (a) Alkenes used in the epoxidation reaction, (b) conversion and selectivity in epoxidation over CoOCl/BVO, and (c) proposed mechanism of epoxidation *via in situ* generated HOCl. Reproduced from ref. 34. Copyright 2024, Wiley-VCH. (d) Proposed mechanism of the selective oxidation of methane over BiOCl-OV. Reproduced from ref. 149. Copyright 2023, Elsevier.

to secondary alcohols, like 2-propanol, with 92% selectivity to acetone.

$$Cl^- + H_2O \rightarrow HOCl + H^+ + 2e^- \quad (40)$$

$$CH_3CH_2OH + HOCl \rightarrow CH_3CHO + H^+ + Cl^- + H_2O \quad (41)$$

$$CH_3CHO + \frac{1}{2}O_2 \rightarrow CH_3COOH \quad (42)$$

The selective photocatalytic oxidation of methane to methanol is highly desirable to simultaneously mitigate greenhouse gases and to produce fuels, but it is very challenging due to a large energy barrier of C–H activation and bond energy (439 kJ mol^{-1}).[150] Fortunately, active chlorine species can be used to abstract H from CH_4, which can then be oxidised to CH_3OH with 80% selectivity in the presence of H_2O_2. H_2O_2 undergoes decomposition and supplies $^\bullet OH$ and $O_2^{\bullet -}$ radicals. Cl^- oxidation to a $^\bullet Cl$ radical offers an advantage in carrying out CH_4 oxidation in a seawater solution. Wang *et al.* showed that both $Cl^\bullet$ and $^\bullet OH$ are crucial for the conversion of CH_4 to CH_3OH over BiOCl with oxygen vacancies (BiOCl–O_V), where oxygen vacancies (V_O) serve as an active site for Cl^- adsorption (Fig. 17d).[149] $Cl^\bullet$ is required to form a $^\bullet CH_3$ intermediate, which is oxidised by $^\bullet OH$ to yield CH_3OH. Interestingly, pristine BiOCl (without oxygen vacancies) produces Cl_2, which is responsible for halogenated compounds (CH_2Cl_2 and $CHCl_3$), while BiOCl-V_o yields $Cl^\bullet$, which is responsible for H abstraction from CH_4. In another work, the same group also reported the formation of diethyl ether ($C_4H_{10}O$) as the majority and other chlorinated products such as CH_2Cl_2, $CHCl_3$ and $C_2H_4Cl_2O$ in synthetic seawater.[56]

Overall, *in situ* generated RCS are key for the oxidation and conversion of organic compounds. Importantly, RCS shows high selectivity towards particular products, which renders COR advantageous and promising for selective oxidation.

(d) Oxidation and chlorination of amines and sulfides

A strong oxidising capability of reactive chlorine species (Cl_2 and HOCl) renders it suitable for various organic transformations, including the oxidation of amines and sulfides. Notably, HOCl can initiate oxidative fragmentation without incorporating Cl atoms into the final products. For example, Hull *et al.* reported the mechanism of triethylenediamine oxidation by HOCl to produce piperazine, which can be further oxidised to ethylenediamine and formaldehyde.[151] The first step usually involves hydrogen abstraction and the inclusion of a chlorine atom in amines. Aldehydes seem to be a common product of amine oxidation by HOCl, as also observed in the reaction of aminoalcohols with HOCl. Interestingly, kinetic studies have shown that tertiary amines react much faster with HOCl than primary and secondary amines.[152]

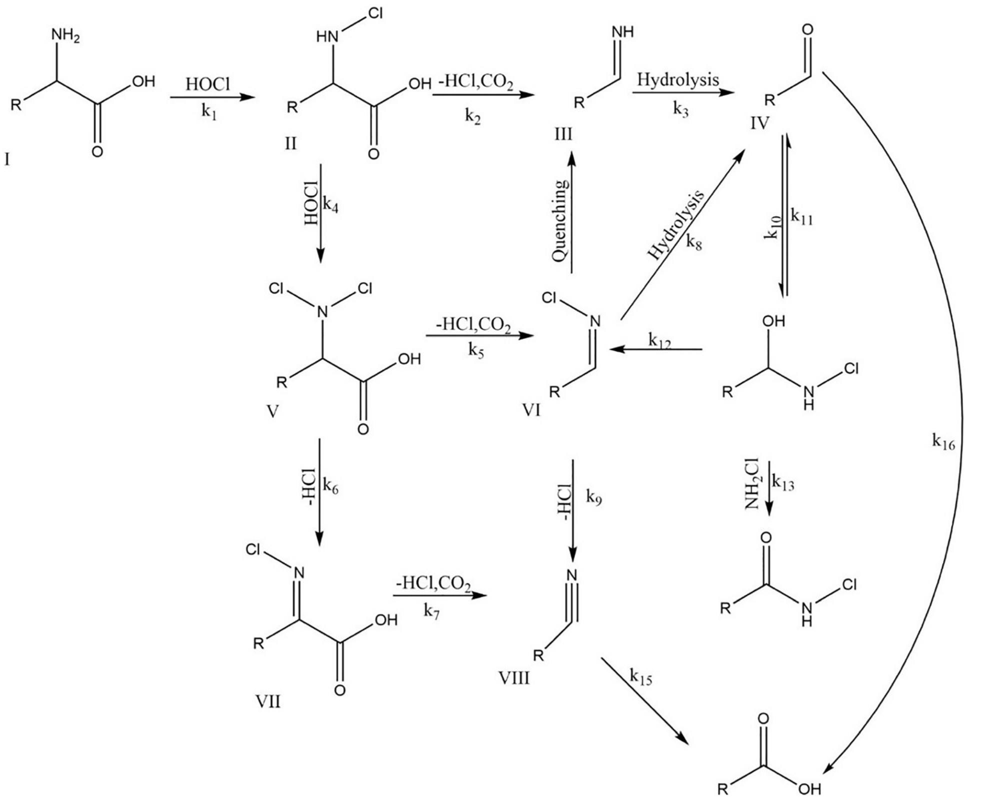

Scheme 2 Mechanistic pathways of the oxidation of amino acids by HOCl with the liberation of CO_2 and formation of aldehyde and nitrile. Reproduced from ref. 158. Copyright 2017, the American Chemical Society.

Reactions between organic amines and RCS often yield the corresponding chlorinated amine (N–Cl) compounds, which are significant in biochemistry and environmental chemistry. Organic amines, like amino acids, are often present in wastewater and sewage sludge, which are treated with HOCl. Reactions between amino acids and peptides with HOCl proceed readily. The importance of the reaction between RCS and amino acids in enzymes in bacteria is paramount to understanding bacterial deactivation and inactivation in wastewater treatment. A free amino group in amino acids reacts with HOCl to yield unstable chloroamine intermediates ($RNHCl/RNH_2^+Cl$), which subsequently decompose to NH_3, CO_2, nitriles, and aldehydes.[153–156] Notably, N-chloro derivatives form rapidly from the reaction of amino acids and HOCl and decompose slowly in multisteps (Scheme 2). Although the products of amine oxidation by HOCl are well known and well characterised, the mechanism remains elusive and less understood. Hawkins and Davies verified the formation of radical intermediates from the decomposition of chloroamines and chloroamides by electron paramagnetic resonance (EPR).[157] However, several dipeptides were found to be resistant to HOCl at room temperature.

N-chlorination reactions render it suitable for the application of *in situ* generated RCS by photocatalytic and photoelectrochemical means. Ding *et al.* demonstrated enantioselective chlorofunctionalization of *N*-substituted amides using *in situ* generated HOCl.[159] The role of HOCl is identified as a proton donor and a hypochlorite source. It is therefore expected that *in situ* generated RCS from seawater splitting facilitates organic transformations of amine compounds.

Hydrogen sulfide (H_2S) is a weak acid and toxic gas, which is produced as an emission gas from chemical, oil and gas industries. Chemical scrubbing is a typical method for removing H_2S emissions using a gas–liquid contactor containing an oxidant, such as HOCl or H_2O_2.[160] The oxidation of H_2S is a fast reaction, follows a complex mechanism, and is strongly pH dependent. The nucleophilic characteristics of HS^- and S^{2-} (sulfide) make it reactive to electrophilic HOCl. Sulfide in H_2S is oxidised by HOCl to yield elemental sulfur (S) and chloride (Cl^-).[161] Reacting emitted H_2S with *in situ* generated HOCl may pave the way toward efficient H_2S removal with low capital and operating costs. Moreover, the reactivity between H_2S and HOCl helps us to understand the role of HOCl in neurodegenerative diseases associated with the H_2S concentration in the brain.[162]

The oxidation products of organic sulfur compounds depend on the type of sulfur. The reaction rate for a few sulfur compounds was established in the following order: thiol > thioether > sulfoxide. Sulfides are oxidised to sulfoxides, and overoxidation in excess of chlorine yields sulfones, while thiols form disulfides and gradually transform to sulfonic acids.[163] Meanwhile, thioethers are oxidised to sulfoxides.[164] Sulfur-containing compounds, such as thiourea, thiosulfate and thioglycolate, are reactive towards oxidation by HOCl. For instance, Stanbury's group reported that the reaction rate of these sulfur compounds with HOCl is much more rapid than using H_2O_2 and $[Pt(CN)_4Cl_2]^{2-}$ oxidants, highlighting the former's superior oxidative capability owing to the highly electrophilic HOCl.[165] Moreover, the solubility of HOCl in polar organic solvents, such as CH_2Cl_2, renders it advantageous in various organic reactions because no phase transfer catalysts are required for the oxidation process.

(e) Photocatalytic CO_2 reduction

Photocatalytic CO_2 reduction (PCR) represents a sustainable carbon cycling system and a clean route to mitigate the CO_2 level in the atmosphere and produce high value-added chemicals and fuels, like CO, CH_4, and CH_3OH. However, research in PCR generally employs water as an electron donor; thus, the non-trivial role of other photooxidation half-reactions is often overlooked. It has been shown that Cl^- oxidation enhances activity and selectivity toward specific products in PCR. Coupling CO_2 reduction to CO and Cl^- oxidation to Cl_2 (or HOCl) is kinetically favoured because both half-reactions involve a stoichiometric amount of charge carriers, *i.e.* two electrons and two holes. Layered-double hydroxides (LDHs) with remarkable adsorption capacities, diverse compositions and ions, and tunable optical and photoelectrochemical properties are widely used for CO_2 capture and gaining attention for photocatalytic CO_2 reduction.[166] Ni–Al LDHs exhibit a selective formation of CO (86%) from photoreduction of CO_2 with almost twice the CO_2 yield in aqueous NaCl (0.1 M) compared to pure water; the remaining 14% is H_2 evolution, and no other products, such as CH_4, CH_3OH and HCOOH, are detected in the reaction.[19] However, the mechanism and the underlying reason the addition of Cl^- ions favours higher activity and selectivity are not addressed in the work, except that Cl^- acts as a hole scavenger to form HOCl and thus remains elusive.

Recently, surface Lewis basicity has been introduced by doping the {001} facets in BiOCl with nitrogen (N-BiOCl) to enhance CO_2 adsorption and activation for PCR in natural seawater (The Yellow Sea, China, was used as an example).[72] The near stochiometric production rates of HOCl and CO under visible light are 83.2 and 92.8 μmol g^{-1} h^{-1}, respectively, with product selectivity above 90% for both HOCl and CO (Fig. 18a and b). The reaction pathway attributes CO_2 reduction on the {001} facets, where photoelectrons are accumulated, and HOCl formation to be most likely on the lateral {110}/{010} facets *via* self-oxidation of lattice Cl^- ions. In another work, Wang *et al.* observed that the $CO_3{}^{2-}$ intermediate in PCR may participate in the BiOCl interlayers, causing distortion and exchange of Cl^- ions in BiOCl as evidenced by XRD patterns, Raman and XPS measurements (Fig. 18c–f).[73] However, no reduction products (*e.g.* CO, CH_4, and CH_3OH) were quantified in the study.

Notably, the findings from photocatalytic COR improving the photoactivity and selectivity in PCR have led researchers to design novel Cl-modified photocatalysts through surface modification, grafting or doping with Cl^- ions.[167–169] Although these works are not related to PC or PEC seawater splitting or Cl_2/HOCl formation, they highlight how the progress in seawater splitting has impacted other photocatalytic reactions and photocatalyst designs.

10. Challenges and future direction

The competing reactions between oxygen evolution reaction (OER) and chlorine evolution reaction (CER) determine the selectivity in photo(electro)catalytic seawater splitting. A considerable number of factors govern the selectivity of CER, including the Cl^- concentration, pH of the electrolyte, electrocatalyst, and applied potential. In acidic and near neutral media, CER dominates over OER, while OER is preferred at high pH. Thus, acidification is often performed to enhance CER selectivity. In addition, the free energy difference in the –OCl and –OOH intermediates is used as the selectivity descriptor to predict the selectivity of CER and OER. For example, the stabilisation energy of OCl_{ad} is used as an activity descriptor to evaluate the effectiveness of CER electrocatalysts and is further employed to explain the superior activity of RuO_2 than IrO_2.[170] DFT calculations by Hansen *et al.* disclosed that Cl^- is adsorbed on the O-covered rutile surfaces spontaneously forming an –OCl intermediate.[43] Moreover, CER only involves a single intermediate compared to OER that proceeds *via* three intermediates, giving an advantage to the former reaction. Similarly, *ab initio* density functional theory (DFT) was performed using different RuO_2 crystal facets to investigate the overpotential of CER and OER.[171] RuO_2(101) was found to promote CER, and RuO_2(001) preferentially catalysed OER.

Zeradjanin *et al.* proposed a dynamic catalytic descriptor based on vibrational frequencies of the crystal lattice from *in situ* Raman spectroscopy and electrochemical methods.[172] The Raman shifts of metal–oxide bonds form a volcano plot, where the most active electrocatalysts with low overpotential for CER are RuO_2 and IrO_2, located close to the Cl–O bond (725 cm^{-1}) found in HOCl (Fig. 19a). The volcano plot rationalises the established knowledge that RuO_2 and IrO_2 are the best performing electrocatalysts in dimensionally stable anodes (DSAs) for the chlor-alkali process. The authors also concluded that CER is a resonance phenomenon in which the catalyst surface, intermediates and products exhibit vibrational bonds with a similar frequency. It is therefore possible to predict and screen the best performing catalysts based on Raman spectroscopy and electrochemical studies where the vibrational modes of the metal–oxide (M–O) bond are close to those of the Cl–O bond. Notably, the Raman frequency and the length of the M–O bond are inversely proportional, which uses X-ray absorption spectroscopy (EXAFS/XANES) in determining the bond lengths useful for predicting suitable co-catalysts for CER.[173]

Another key parameter for efficient and robust electrocatalysts for CER is high conductivity to survive anodic conditions. The two best-performing and most employed electrocatalysts in the chlor-alkali process, RuO_2 and IrO_2, are metallic oxides (Fig. 19b). Rutile RuO_2 has partially filled 4d orbitals and therefore exhibits metallic conductivity.[174] For IrO_2, a large 5d orbitals overlap which is comparable to the Ir–O bond distance

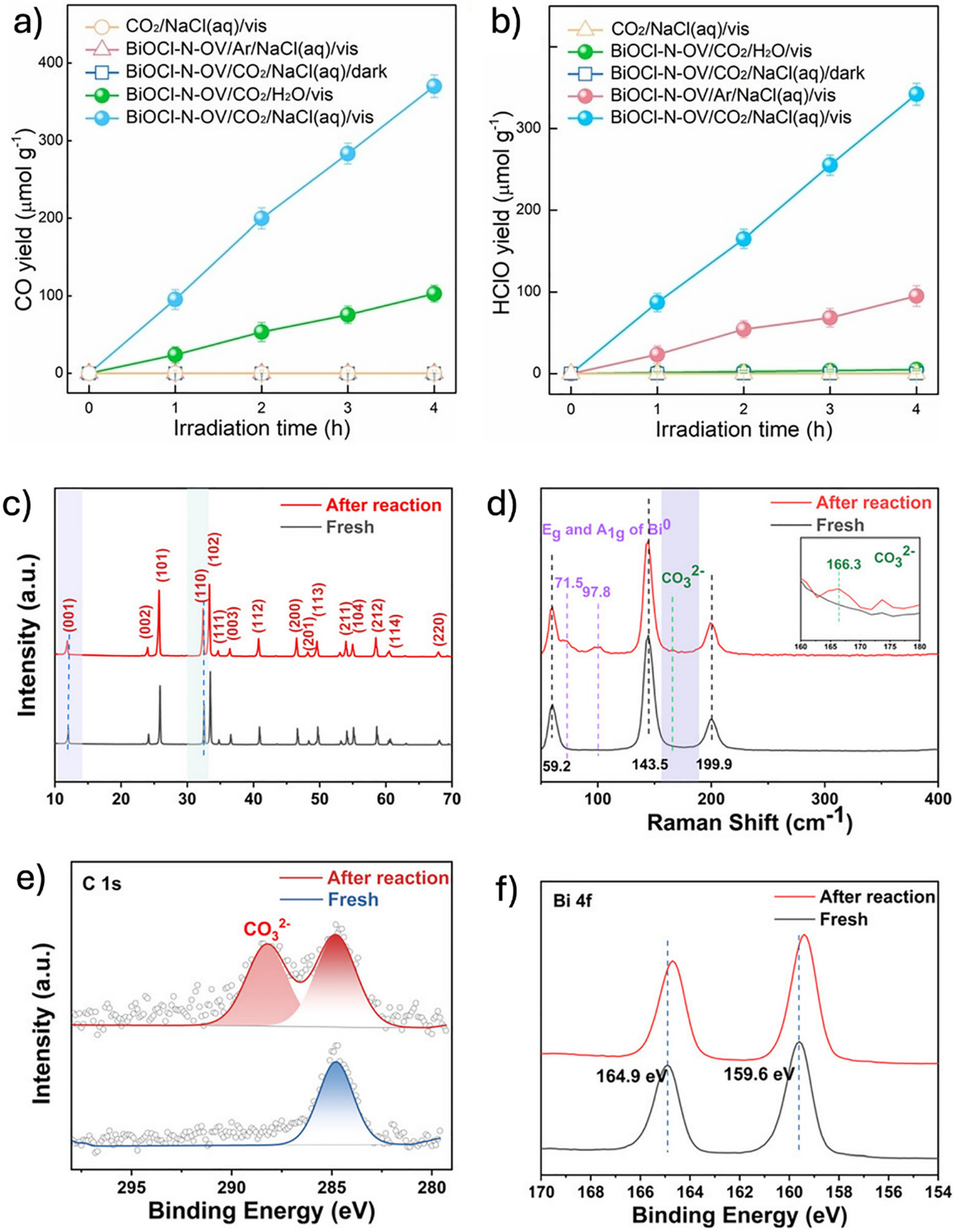

Fig. 18 Photocatalytic formation of (a) CO and (b) HOCl over N-BiOCl. Reproduced from ref. 72. Copyright 2023, Wiley-VCH. Characterizations of the BiOCl photocatalysts before and after reactions: (c) XRD patterns, (d) Raman spectra, (e) C 1s XP spectra, and (f) Bi 4f XP spectra. Reproduced from ref. 73. Copyright 2023, Wiley-VCH.

renders it metallic oxide.[175] Furthermore, low CER overpotential was observed for perovskite oxides with metallic conductivity, such as $La_{0.5}Sr_{0.5}CoO_3$ and $LaNiO_3$. It should be noted that mixed metal oxides (MMO) usually contain a TiO_2 semiconductor to improve the stability of DSAs while contributing little to their activity and selectivity. Metallic conductivity serves as a useful guide for exploring and designing suitable co-catalysts for photoanodes in CER.

A reasonable direction for exploring novel photocatalysts and photoanodes would involve the utilisation of *in situ* spectroscopy and electrochemical measurements to probe the vibrational frequencies and correlate them with the corresponding CER overpotential. This is possible for coordination polymers, such as metal–organic frameworks (MOFs) and covalent organic frameworks (COFs). The presence of metal nodes in MOFs and organic functional groups in COFs opens a new avenue for establishing similar overpotential-based volcano plots. Moreover, *in situ* Raman and infrared spectroscopy have proved advantageous in identifying intermediates and their binding with specific metal nodes or functional groups.

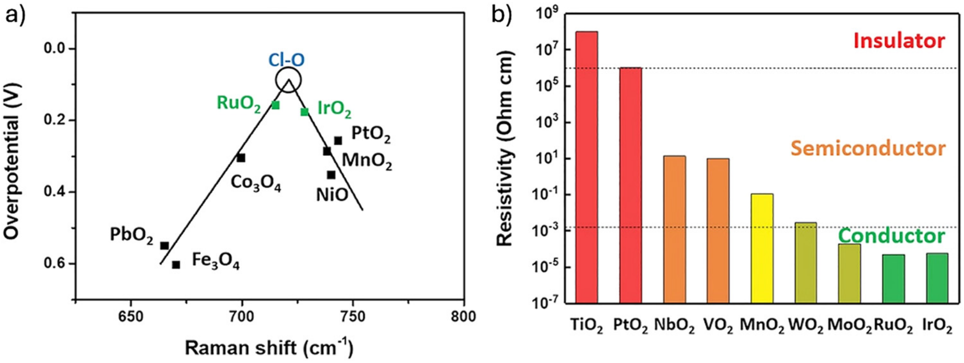

Fig. 19 (a) Overpotential of CER as a function of Raman shift for several metal oxides and (b) resistivity of several metal oxides. Reproduced from ref. 40. Copyright 2023, Wiley-VCH.

Currently, the lack of such data restricts the prediction and knowledge-based design of effective novel photocatalysts for CER.

Computational studies provide a means of describing phenomena on the surface of photocatalysts at the molecular level, which can complement and help understand experimental studies. DFT with thermodynamic considerations was utilised to establish a correct selectivity descriptor for CER. Exner unravelled that the formation free-energy of oxygen with respect to hydroxide, $\Delta G_{\text{O–OH}}$, provides a correct description of the activity (or selectivity) trend for CER than the free-energy of binding energy of oxygen (ΔG_{O}), which is typically used in the oxidation activity of metal oxides.[176] Importantly, the $\Delta G_{\text{O–OH}}$ descriptor has reproduced the activity trends of CER and OER for $RuO_2(110)$ and $IrO_2(110)$ accurately. Because OER and CER compete in an anodic process, both reactions must be considered to reproduce activity trends. The $\Delta G_{\text{O-OH}}$ descriptor is capable of describing both OER and CER activity trends correctly, whereas the ΔG_{O} cannot reproduce OER activity correctly. A prime advantage of using the $\Delta G_{\text{O–OH}}$ descriptor is that the values can be computed by *ab initio* calculations and verified by cyclic voltammetry.[177]

Besides a direct Cl^- adsorption to an oxygen atom in rutile metal oxides, Cl^- can also bind to two oxygen atoms, forming ClO_2^- in CER.[43] Exner included this possibility of ClO_2^- in his unifying material-screening framework, which includes overpotential, kinetics and electrochemical-step symmetry index, to comprehend the selectivity issues in CER.[178] Based on this thermodynamic consideration, the formation of –Cl intermediate (*i.e.* O^cCl, where O^c is a coordinatively unsaturated oxygen atom in metal oxides) should be promoted over –OCl adsorbate (*i.e.* $O^c{}_2Cl$) to enhance the Cl_2/HOCl selective formation. The implication of this finding is to search for and design novel photocatalysts and photoelectrodes that can stabilise a Cl^- intermediate for enhanced Cl_2 selectivity.

In many scenarios, the active sites that bind to the Cl* intermediate also bind to the OH* intermediate, *i.e.* they both share a common active. Hence, the scaling relationship correlates with CER and OER in the chlor-alkali process. To break this scaling relationship, active sites with larger adsorption energy for OH* must be created to promote selectivity towards CER.[179] Doping RuO_2 that results in an increase in the free energy of the OH* formation leads to an improved selectivity toward CER. For example, DFT calculations reveal that replacing the outermost Ru atoms with Ti atoms through the growth of a TiO_2 monolayer on RuO_2 enhances the CER selectivity by several orders of magnitude.[180] Experimental work has also confirmed that doping is an effective strategy for enhancing CER selectivity.[39,181,182]

Although most computational studies on CER are directed at rutile-based metal oxides, there is limited work on emerging materials, such as covalent-organic frameworks (COFs) and metal–organic frameworks (MOFs). Future direction should be dedicated to computing the free-energy of binding energy of Cl^- with N, S, and O atoms in organic functional groups and establishing the corresponding overpotential-based volcano plots because the findings will provide a knowledge-based guideline for rational design of efficient COFs and MOFs for CER. Furthermore, the findings from computational work can be validated by experimental techniques, such as infrared, Raman and nuclear magnetic resonance spectroscopy.

Photocatalytic Cl_2/HOCl production from seawater splitting is still at an early stage of development. In what historically started as a hole scavenger in photocatalytic water splitting using seawater or aqueous seawater solution, the oxidation of Cl^- to Cl_2/HOCl has emerged as a new direction in photocatalysis research for the past decade. Early works attempted to enhance the selectivity of oxidation half-reaction towards water oxidation, neglecting the potential of Cl^- oxidation to RCS (Cl_2/HOCl). The challenging issues in overall water splitting, low economic value of molecular O_2 and scarcity of pure/fresh water have urged researchers to assess other oxidation products that are kinetically favoured and have a high value-added.[6] More importantly, PC and PEC seawater splitting have the potential to replace the energy-intensive conventional, industrial chlor-alkaline process in Cl_2/HOCl production.

PC and PEC Cl_2/HOCl production coupled with H_2 evolution at the anode is a novel strategy for simultaneously generating clean energy and commodity chemicals from widely abundant seawater or saltwater. In natural seawater, dissolved CO_2 could be an advantage in consuming photoexcited electrons, thereby suppressing the recombination of charge carriers and avoiding the continuous supply of O_2 as an electron scavenger. However, dissolved CO_2 forms carbonic acid (H_2CO_3) and HCO_3^-, in which the carbonate anion (CO_3^{2-}) is a good hole scavenger, as reported by Hiroaki Tada.[183] Therefore, there is a competing Cl^- and CO_3^{2-} oxidation in PC or PEC systems. Further work should explore PC or PEC Cl_2/HOCl oxidation in natural seawater/saltwater to investigate the effects of other ions and factors affecting the selectivity in Cl^- oxidation. Importantly, such work using natural and/or synthetic seawater will bring us closer toward a practical application.

Given that HOCl easily decomposes under exposure to UV light, the use of wide band gap photocatalysts should be minimized to achieve a high production rate and yield of HOCl. Nonetheless, good photocatalysts for COR are still dominated by wide band gap photocatalysts, like TiO_2 and BiOCl (band gap > 3.0 eV), which render visible-light-driven photocatalysts less explored. Many earth-abundant, visible light photocatalysts have appropriate valence bands (>1.40 V *vs.* RHE), such as g-C_3N_4, CdS, TaON, MoS_2 and Fe_2O_3, or other polymeric photocatalysts that remain relatively unexplored for COR and thus open a window of opportunity for catalyst development. Furthermore, photocatalysts for Cl^- oxidation should consist of few (precious) metals because the acidic medium, resulting from the formation of HOCl, tends to dissolve metals under photoirradiation. Sayama's group observed a dissolution of Pt co-catalyst, forming soluble $PtCl_6^{2-}$ through a reaction with evolved Cl_2, during photoirradiation in seawater splitting.[58] The same group also reported a dissolution of Mn co-catalysts under photocatalytic conditions.

Except for limited photocatalytic materials, such as BiOCl and $BiVO_4$, the facet-dependent reactivity and selectivity of Cl/HOCl formation remain underexplored. Different crystal facets have different surface energetics and accumulate different charge carriers caused by the internal electric field (IEF).[184] However, the selectivity of oxidation-favoured facets is complicated by competitive water and chloride oxidation reactions. Theoretical simulations of specific facets can reveal the relative activation energy or overpotential for Cl^- oxidation. Moreover, the intermediates in COR have not yet been fully clarified, thus presenting an opportunity for further theoretical work.

Currently, despite numerous investigations on PC and PEC of Cl_2/HOCl formation using various photocatalysts and co-catalysts, the knowledge about the active sites remains elusive. Except for a few photocatalytic materials, like BiOCl and AgCl as well as $Co_2(OH)_3Cl$ co-catalyst, where participation of the lattice Cl^- in COR *via* the Mars–van Krevelen mechanism is verified, the active sites in many other catalytic materials are unknown. Moreover, the postulate of the existence of Co–Cl interaction when using a CoO_x co-catalyst and/or overlayer has not been successfully verified by X-ray photoelectron spectroscopy.[95] CoO_x is a well-known electrocatalyst in oxygen evolution reaction (OER);[185–187] therefore, understanding the nature of the catalytically active sites and interaction with Cl^- is of paramount importance to tune the selectivity between OER and COR. Additionally, it has been reported that Cl^- can stabilise oxygen vacancies in TiO_2 and BiOCl, thereby promoting the formation of RCS or $Cl^\bullet$ radicals for photocatalytic oxidation and degradation.[149,188] It has also been suggested that Cl^- interacts favourably with the TiO_2 surface although this interaction has not been verified by physical or electrochemical characterizations.[139] Future work should disclose the interaction and/or adsorption of Cl^- with the surface of photocatalysts. Currently, such limitations impede the knowledge-driven design and optimization of selective, active, and stable photocatalysts for COR.

We highlight that PC or PEC seawater splitting represents another type of artificial solar photosynthesis where H_2 evolution at the cathode can be coupled with Cl_2/HOCl formation at

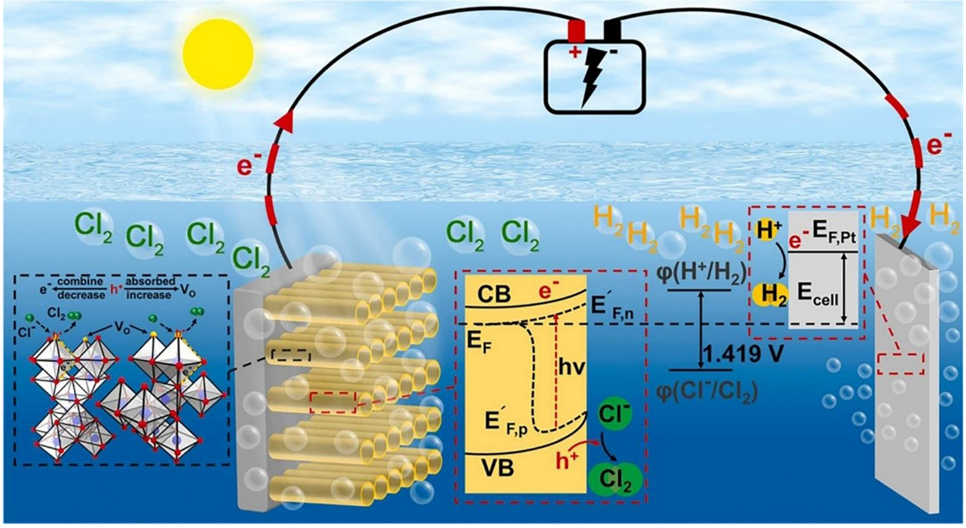

Fig. 20 Schematic of the simultaneous Cl_2 and H_2 evolution at a TiO_2 photoanode and a Pt cathode, respectively. Reproduced from ref. 44. Copyright 2023, Elsevier.

the photoanode.[33,44,64] More importantly, the separation of the evolution of H_2 and Cl_2 in PEC systems enables a direct collection of both gases for further utilisation or storage (Fig. 20). Such a strategy potentially circumvents the low-economic value of O_2 and sluggish kinetics of O_2 evolution in water-splitting. Therefore, PC and PEC seawater splitting present a feasible green alternative and economical method for renewable energy and CO_2 emission mitigation compared to the traditional chlor-alkaline process.

Finally, we offer a perspective on coupled redox reactions involving a COR half-reaction. The other half-reduction reactions are not limited to H_2 evolution or CO_2 reduction, as discussed above. Very recently, Chen and Zhang constructed $In_2S_3/MnIn_2S_4$-based photoanode and photocathode for simultaneous production of HOCl and H_2O_2, respectively, which highlighted a promising approach for the production of fine chemicals *via* PEC.[189] N_2 reduction to NH_3 has been another intense area of photocatalysis research for producing energy carriers. Shiraishi *et al.* demonstrated photocatalytic N_2 fixation to produce NH_3 in a seawater solution over oxygen-deficient BiOCl–O_v with solar-to chemical conversion of 0.05% HOCl.[65] Moreover, halogenation of alkanes into organic halides – important industrial and medical chemicals – has been reported using a V_o-rich TiO_2 photoanode.[188] These findings open an avenue for broad, significant impacts of Cl_2/HOCl production, photodegradation of pollutants, production of high value-added chemicals, and artificial photosynthesis involving the production of clean energy. Progress in COR *via* seawater splitting is still in its infancy and offers much room for development in the field.

More importantly, for remote areas that lack water treatment facilities, PC and PEC production of Cl_2/HOCl using natural seawater/saltwater is a sustainable method for on-site and rapid production of Cl_2/HOCl for treating drinking water and sanitizing purposes. It is undoubtedly that PC and PEC seawater splitting to produce Cl_2/HOCl addresses at least four SDGs' goals: Good Health and Well-being (#3), Clean Water and Sanitization (#6), Affordable and Clean Energy (#7), and Climate Action (#13).

Conflicts of interest

There are no conflicts to declare.

Abbreviation

AQY	Apparent quantum yield
COR	Chloride (Cl^-) oxidation reaction
DFT	Density-functional theory
DPD	*N,N*-diethyl-p-phenylenediamine
DSA	Dimensionally stable anode
EIS	Electrochemical impedance spectroscopy
ETL	Electron transport layer
FE	Faradaic efficiency
HTL	Hole transport layer
IEF	Internal electric field
IET	Interfacial electron transfer
IPCE	Incident photon conversion efficiency
LDH	Layered double hydroxide
LSPR	Localised surface plasmon resonance
LSV	Linear sweep voltammetry
MSI	Metal-support interaction
OER	Oxygen evolution reaction
PL	Photoluminescence
P25	TiO_2 with anatase (70%–80%) and rutile (20%–30%) phases
PCR	Photocatalytic CO_2 reduction
PWS	Photocatalytic water splitting
RCS	Reactive chlorine species
ROS	Reactive oxygen species
SCC	Solar-to-chemical conversion
STH	Solar-to-hydrogen
V_o	Oxygen vacancies

Data availability

No primary research results, software or code have been included and no new data were generated or analysed as part of this review.

Acknowledgements

RHA thanks Greg Metha (Adelaide University) and Gunther Andersson (Flinders University) for the fruitful discussions on Sayama's paper (https://doi.org/10.1021/acsenergylett.8b00318), which motivated this work on photocatalytic production of high value-added chemicals beyond water splitting. This project was financially supported by KAUST (BAS/1/1433-01-01 and FCC/1/5937-19-01).

References

1 A. Fujishima and K. Honda, *Nature*, 1972, **238**, 37–38.
2 R. Marschall, *Eur. J. Inorg. Chem.*, 2021, 2435–2441.
3 C. R. Lhermitte and K. Sivula, *ACS Catal.*, 2019, **9**, 2007–2017.
4 Z. Guo, Y. Tian, J. He and H. Song, *ChemCatChem*, 2024, e202301595.
5 S. Cao, T. Sun, Y. Peng, X. Yu, Q. Li, F. L. Meng, F. Yang, H. Wang, Y. Xie, C.-C. Hou and Q. Xu, *Small*, 2024, **20**, 2404285.
6 K. Sayama, *ACS Energy Lett.*, 2018, **3**, 1093–1101.
7 W. A. Rutala and D. J. Weber, *Clin. Microbiol. Rev.*, 1997, **10**, 597–610.
8 World Health Organization, Guidelines for drinking-water quality, 4th edition, incorporating the 1st addendum, World Health Organization, 2017.
9 S. Iguchi, Y. Miseki and K. Sayama, *Sustainable Energy Fuels*, 2018, **2**, 155–162.

10 R. Pang, Y. Miseki, S. Okunaka and K. Sayama, *ACS Sustainable Chem. Eng.*, 2020, **8**, 8629–8637.

11 R. K. B. Karlsson and A. Cornell, *Chem. Rev.*, 2016, **116**, 2982–3028.

12 Z. Chen, J. J. Concepcion, N. Song and T. J. Meyer, *Chem. Commun.*, 2014, **50**, 8053–8056.

13 M. Busch, N. Simic and E. Ahlberg, *Phys. Chem. Chem. Phys.*, 2019, **21**, 19342–19348.

14 M. Luna-Trujillo, R. Palma-Goyes, J. Vazquez-Arenas and A. Manzo-Robledo, *J. Electroanal. Chem.*, 2020, **878**, 114661.

15 C. Zhao, Z. Ding, K. Zhang, Z. Du, H. Fang, L. Chen, H. Jiang, M. Wang and M. Wu, *Nano-Micro Lett.*, 2025, **17**, 113.

16 K. Mase, M. Yoneda, Y. Yamada and S. Fukuzumi, *Nat. Commun.*, 2016, **7**, 11470.

17 L. Huang, R. Li, R. Chong, G. Liu, J. Han and C. Li, *Catal. Sci. Technol.*, 2014, **4**, 2913–2918.

18 J. Johnston, C. O'Rourke and A. Mills, *Phys. Chem. Chem. Phys.*, 2023, **25**, 31825–31835.

19 S. Iguchi, K. Teramura, S. Hosokawa and T. Tanaka, *Phys. Chem. Chem. Phys.*, 2015, **17**, 17995–18003.

20 G. Hippargi, P. Mangrulkar, A. Chilkalwar, N. Labhsetwar and S. Rayalu, *Int. J. Hydrogen Energy*, 2018, **43**, 6815–6823.

21 X. Guan, F. A. Chowdhury, N. Pant, L. Guo, L. Vayssieres and Z. Mi, *J. Phys. Chem. C*, 2018, **122**, 13797–13802.

22 V.-H. Dang, T.-A. Nguyen, M.-V. Le, D. Q. Nguyen, Y. H. Wang and J. C.-S. Wu, *Chem. Eng. J.*, 2024, **484**, 149213.

23 F. Dingenen and S. W. Verbruggen, *Renewable Sustainable Energy Rev.*, 2021, **142**, 110866.

24 M. S. Yesupatham, A. Augustin, N. Agamendran, B. Honnappa, M. Shanmugam, P. J. J. Sagayaraj, G. Thennarasu, N. C. Sagaya Selvam and K. Sekar, *Sustainable Energy Fuels*, 2023, **7**, 4727–4757.

25 B. Rao, N. Estrada, S. McGee, J. Mangold, B. Gu and W. A. Jackson, *Environ. Sci. Technol.*, 2012, **46**, 11635–11643.

26 S. Dresp, F. Dionigi, M. Klingenhof and P. Strasser, *ACS Energy Lett.*, 2019, **4**, 933–942.

27 R. Vogt and R. N. Schindler, *J. Photochem. Photobiol., A*, 1992, **66**, 133–140.

28 J. Fang, Y. Fu and C. Shang, *Environ. Sci. Technol.*, 2014, **48**, 1859–1868.

29 X. Li, M. Kan, T. Wang, Z. Qin, T. Zhang, X. Qian, Y. Kuwahara, K. Mori, H. Yamashita and Y. Zhao, *Appl. Catal., B*, 2021, **296**, 120387.

30 M. S. Koo, X. Chen, K. Cho, T. An and W. Choi, *Environ. Sci. Technol.*, 2019, **53**, 9926–9936.

31 M. Szabó, N. Lihi, N. Simic and I. Fábián, *Chem. Eng. Res. Des.*, 2021, **169**, 97–102.

32 T. Okada, M. Kodera, Y. Miseki, H. Kusama, T. Gunji and K. Sayama, *Chem. Commun.*, 2024, **60**, 3299–3302.

33 M. Jadwiszczak, K. Jakubow-Piotrowska, P. Kedzierzawski, K. Bienkowski and J. Augustynski, *Adv. Energy Mater.*, 2020, **10**, 1903213.

34 Y. Yang, X. Yuan, Q. Wang, S. Wan, C. Lin, S. Lu, Q. Zhong and K. Zhang, *Angew. Chem., Int. Ed.*, 2024, **63**, e202314383.

35 Y. Wang, Y. Wang, J. Zhao and Y. Xu, *Appl. Catal., B*, 2021, **299**, 120676.

36 Y. Zhou, Z. Xu, L. Tang, J. Qin, G. Lu, H. Dong, Z. Bian and M. Zhu, *Environ. Sci. Technol.*, 2024, **58**, 6049–6057.

37 J. N. Hausmann, R. Schlögl, P. W. Menezes and M. Driess, *Energy Environ. Sci.*, 2021, **14**, 3679–3685.

38 J. Yu, B.-Q. Li, C.-X. Zhao and Q. Zhang, *Energy Environ. Sci.*, 2020, **13**, 3253–3268.

39 Y. Wang, Y. Liu, D. Wiley, S. Zhao and Z. Tang, *J. Mater. Chem. A*, 2021, **9**, 18974–18993.

40 S. Choi, W. I. Choi, J.-S. Lee, C. H. Lee, M. Balamurugan, A. D. Schwarz, Z. S. Choi, H. Randriamahazaka and K. T. Nam, *Adv. Mater.*, 2023, **35**, 2300429.

41 K. S. Exner, J. Anton, T. Jacob and H. Over, *Electrocatalysis*, 2015, **6**, 163–172.

42 L. I. Krishtalik, *Electrochim. Acta*, 1981, **26**, 329–337.

43 H. A. Hansen, I. C. Man, F. Studt, F. Abild-Pedersen, T. Bligaard and J. Rossmeisl, *Phys. Chem. Chem. Phys.*, 2010, **12**, 283–290.

44 Y. Ye, B. Liao, M. Li, M. Mai, L. Zhang, L. Ma, D. Lin, J. Zhao, D. Chen and X. Ma, *J. Alloys Compd.*, 2023, **947**, 169480.

45 R. Sakamoto, D. Horiguchi, T. Ikegami, M. Ishiyama, M. Shiga, K. Sasamoto and Y. Katayama, *Anal. Sci.*, 2003, **19**, 1445–1447.

46 Q. Lu, Y. Wang, D. Zhang and H. Cong, *Res. Chem. Intermed.*, 2022, **48**, 29–47.

47 R. Pang, Y. Miseki and K. Sayama, *Catal. Sci. Technol.*, 2022, **12**, 2935–2942.

48 S. Okunaka, Y. Miseki and K. Sayama, *iScience*, 2020, **23**, 101540.

49 Y. Wang, Q. Lu, S. Han, D. Zhang, H. Cong and C. Chen, *Mater. Res. Bull.*, 2023, **166**, 112347.

50 J. Ke, M. Adnan Younis, Y. Kong, H. Zhou, J. Liu, L. Lei and Y. Hou, *Nano-Micro Lett.*, 2018, **10**, 69.

51 J. Sun, Y. Chi, W. Wang, S. Zhan and F. Zhou, *React. Kinet., Mech. Catal.*, 2024, **137**, 1239–1253.

52 S. Han, Y. Wang, D. Zhang and H. Cong, *Chem. Commun.*, 2023, **59**, 6857–6860.

53 Y. Wang, S. Han, Q. Lu, D. Zhang, J. Wang and P. He, *ChemSusChem*, 2024, e202400795.

54 Y. Li, W. Nie, Y. Liu, D. Huang, Z. Xu, X. Peng, C. George, C. Yan, Y. J. Tham, C. Yu, M. Xia, X. Fu, X. Wang, L. Xue, Z. Wang, Z. Xu, X. Chi, T. Wang and A. Ding, *Environ. Sci. Technol. Lett.*, 2020, **7**, 70–75.

55 A. Fujishima, X. Zhang and D. A. Tryk, *Surf. Sci. Rep.*, 2008, **63**, 515–582.

56 H. Wang, Z. Han, Y. Zhou, X. Liu, D. Zeng, W. Wang, D. Sarker, L. Zhang and W. Wang, *Appl. Catal., B*, 2021, **297**, 120436.

57 T. R. Harris-Lee, Y. Zhang, C. R. Bowen, P. J. Fletcher, Y. Zhao, Z. Guo, J. W. F. Innocent, S. A. L. Johnson and F. Marken, *Electrocatalysis*, 2021, **12**, 65–77.

58 T. Okada, M. Kodera, Y. Miseki, T. Gunji and K. Sayama, *J. Catal.*, 2025, **443**, 115969.

59 K. Maeda, K. Teramura, D. Lu, N. Saito, Y. Inoue and K. Domen, *Angew. Chem., Int. Ed.*, 2006, **45**, 7806–7809.

60 K. Maeda, K. Teramura, D. Lu, N. Saito, Y. Inoue and K. Domen, *J. Phys. Chem. C*, 2007, **111**, 7554–7560.

61 M. Yoshida, K. Takanabe, K. Maeda, A. Ishikawa, J. Kubota, Y. Sakata, Y. Ikezawa and K. Domen, *J. Phys. Chem. C*, 2009, **113**, 10151–10157.

62 T. Takata, J. Jiang, Y. Sakata, M. Nakabayashi, N. Shibata, V. Nandal, K. Seki, T. Hisatomi and K. Domen, *Nature*, 2020, **581**, 411–414.

63 M. Qureshi, T. Shinagawa, N. Tsiapis and K. Takanabe, *ACS Sustain. Chem. Eng.*, 2017, **5**, 8079–8088.

64 S. Okunaka, T. Nakamura, T. Ikeda, K. Tsuruda and H. Tokudome, *Sustainable Energy Fuels*, 2024, **8**, 745–751.

65 Y. Shiraishi, M. Hashimoto, K. Chishiro, K. Moriyama, S. Tanaka and T. Hirai, *J. Am. Chem. Soc.*, 2020, **142**, 7574–7583.

66 Y. Shiraishi, Y. Shimabukuro, K. Shima, S. Ichikawa, S. Tanaka and T. Hirai, *JACS Au*, 2023, **3**, 1403–1412.

67 J. Li, Y. Yu and L. Zhang, *Nanoscale*, 2014, **6**, 8473–8488.

68 X. Zhao, Z. Zhao-Karger, D. Wang and M. Fichtner, *Angew. Chem., Int. Ed.*, 2013, **52**, 13621–13624.

69 Y. Zhou, H. Wang, X. Liu, D. Zeng, K. Wang, L. Zhang and W. Wang, *Appl. Catal., B*, 2021, **294**, 120265.

70 J. Li, L. Cai, J. Shang, Y. Yu and L. Zhang, *Adv. Mater.*, 2016, **28**, 4059–4064.

71 Z. Xu, L. Tang, Y. Zhou, G. Lu, H. Dong and M. Zhu, *Chem. Eng. J.*, 2024, **493**, 152589.

72 Y. Shi, H. Shou, H. Li, G. Zhan, X. Liu, Z. Yang, C. Mao, J. Cheng, X. Zhang, Y. Jiang, S. Zhao, J. Wang, X. Liu, L. Song, H. Sun and L. Zhang, *Angew. Chem., Int. Ed.*, 2023, **62**, e202302286.

73 J. Wang, L. Zhang, R. Li, D. Zeng, W. Wang and W. Wang, *Chem. – Eur. J.*, 2023, **29**, e202301457.

74 J. Desilvestro and M. Grätzel, *J. Electroanal. Chem. Interfacial Electrochem.*, 1987, **238**, 129–150.

75 M. Parvin, I. Savickaja, S. Tutliene, A. Naujokaitis, R. Ramanauskas, M. Petruleviciene and J. Juodkazyte, *J. Electroanal. Chem.*, 2024, **954**, 118026.

76 J. C. Hill and K.-S. Choi, *J. Phys. Chem. C*, 2012, **116**, 7612–7620.

77 Q. Mi, A. Zhanaidarova, B. S. Brunschwig, H. B. Gray and N. S. Lewis, *Energy Environ. Sci.*, 2012, **5**, 5694–5700.

78 Y. Shi, Y. Li, X. Wei, J. Feng, H. Li and W. Zhou, *J. Electron. Mater.*, 2017, **46**, 6878–6883.

79 S. Ahmed, I. A. I. Hassan, H. Roy and F. Marken, *J. Phys. Chem. C*, 2013, **117**, 7005–7012.

80 S. Y. Jo, J. Y. Bae, J. Y. Park, M. K. Kim, W.-S. Chae, Y.-I. Kim and K. M. Nam, *ACS Appl. Mater. Interfaces*, 2024, **16**, 54864–54872.

81 J. Juodkazytė, M. Petrulevičienė, M. Parvin, B. Šebeka, I. Savickaja, V. Pakštas, A. Naujokaitis, J. Virkutis and A. Gegeckas, *J. Electroanal. Chem.*, 2020, **871**, 114277.

82 S. J. Calero, P. Ortiz, A. F. Oñate and M. T. Cortés, *Int. J. Hydrogen Energy*, 2016, **41**, 4922–4930.

83 A. G. Breuhaus-Alvarez, Q. Cheek, J. J. Cooper, S. Maldonado and B. M. Bartlett, *J. Phys. Chem. C*, 2021, **125**, 8543–8550.

84 D. Chen, Z. Xie, Y. Tong and Y. Huang, *Energy Fuels*, 2022, **36**, 9932–9949.

85 H. Shi, H. Guo, S. Wang, G. Zhang, Y. Hu, W. Jiang and G. Liu, *Energy Fuels*, 2022, **36**, 11404–11427.

86 J. H. Kim and J. S. Lee, *Adv. Mater.*, 2019, **31**, 1806938.

87 X. Zhao, J. Hu, S. Chen and Z. Chen, *Phys. Chem. Chem. Phys.*, 2018, **20**, 13637–13645.

88 M. Chen, X. Chang, C. Li, H. Wang and L. Jia, *J. Colloid Interface Sci.*, 2023, **640**, 162–169.

89 S. Sriwichai, R. Irani, F. Xi, D. Friedrich, C. Höhn, I. Y. Ahmet, N. Wetchakun and F. F. Abdi, *Solar RRL*, 2021, **5**, 2100268.

90 M. Petruleviciene, I. Savickaja, A. Griguceviciene, A. Naujokaitis, R. Ramanauskas and J. Juodkazyte, *J. Photochem. Photobiol., A*, 2023, **443**, 114842.

91 W. Luo, Z. Yang, Z. Li, J. Zhang, J. Liu, Z. Zhao, Z. Wang, S. Yan, T. Yu and Z. Zou, *Energy Environ. Sci.*, 2011, **4**, 4046–4051.

92 S. Iguchi, H. Tateno, S. Takasugi, Y. Miseki and K. Sayama, *Sustainable Energy Fuels*, 2019, **3**, 3441–3447.

93 P. Chen, B. Kang, P. Liu, X. Cheng, S. Zhong, X. Wang and B. Fang, *J. Power Sources*, 2025, **628**, 235860.

94 Z. Xi, C. Zhou, K. Kisslinger, T. Nanayakkara, F. Lu, X. Tong and M. Liu, *ACS Appl. Mater. Interfaces*, 2023, **15**, 49281–49288.

95 S. Okunaka, Y. Miseki and K. Sayama, *Catal. Sci. Technol.*, 2021, **11**, 5467–5471.

96 Y. Zhang, J. Cui and Y. Pei, *Chem. Eng. J.*, 2023, **464**, 142652.

97 Q. Xiong, X. Zhang, Q. Cheng, G. Liu, G. Xu, J. Li, X. Ye and H. Gao, *Nano Res.*, 2021, **14**, 1443–1449.

98 I. Chauhan, K. K. Patra, H. Bajpai, N. B. Mhamane, K. N. Salgaonkar and C. S. Gopinath, *Dalton Trans.*, 2023, **52**, 2051–2061.

99 S. Zhang, I. Ahmet, S.-H. Kim, O. Kasian, A. M. Mingers, P. Schnell, M. Kölbach, J. Lim, A. Fischer, K. J. J. Mayrhofer, S. Cherevko, B. Gault, R. van de Krol and C. Scheu, *ACS Appl. Energy Mater.*, 2020, **3**, 9523–9527.

100 S. Zhang, M. Rohloff, O. Kasian, A. M. Mingers, K. J. J. Mayrhofer, A. Fischer, C. Scheu and S. Cherevko, *J. Phys. Chem. C*, 2019, **123**, 23410–23418.

101 S. Chen and L.-W. Wang, *Chem. Mater.*, 2012, **24**, 3659–3666.

102 A. M. Rassoolkhani, W. Cheng, J. Lee, A. McKee, J. Koonce, J. Coffel, A. H. Ghanim, G. A. Aurand, C. Soo Kim, W. Ik Park, H. Jung and S. Mubeen, *Commun. Chem.*, 2019, **2**, 57.

103 C. Boyle, N. Skillen, H. Q. N. Gunaratne, P. K. Sharma, J. A. Byrne and P. K. J. Robertson, *Mater. Sci. Semicond. Process.*, 2020, **109**, 104930.

104 J. Wu, Y. Tao, C. Zhang, Q. Zhu, D. Zhang and G. Li, *J. Hazard. Mater.*, 2023, **443**, 130363.

105 Z. Hu, H. Wu, S. Li, C. Zhang, R. Liang and M. Zhou, *Chem. Eng. J.*, 2024, **498**, 155308.

106 S.-T. Xiao, S.-M. Wu, L. Wu, Y. Dong, J.-W. Liu, L.-Y. Wang, X.-Y. Chen, Y.-T. Wang, G. Tian, G.-G. Chang, M. Shalom, P. Fornasiero and X.-Y. Yang, *ACS Nano*, 2023, **17**, 18217–18226.

107 H. Nishiyama, T. Yamada, M. Nakabayashi, Y. Maehara, M. Yamaguchi, Y. Kuromiya, Y. Nagatsuma, H. Tokudome, S. Akiyama, T. Watanabe, R. Narushima, S. Okunaka, N. Shibata, T. Takata, T. Hisatomi and K. Domen, *Nature*, 2021, **598**, 304–307.

108 Y. Goto, T. Hisatomi, Q. Wang, T. Higashi, K. Ishikiriyama, T. Maeda, Y. Sakata, S. Okunaka, H. Tokudome, M. Katayama, S. Akiyama, H. Nishiyama, Y. Inoue, T. Takewaki, T. Setoyama, T. Minegishi, T. Takata, T. Yamada and K. Domen, *Joule*, 2018, **2**, 509–520.

109 T. Uekert, M. A. Bajada, T. Schubert, C. M. Pichler and E. Reisner, *ChemSusChem*, 2021, **14**, 4190–4197.

110 S. Dilger, M. Trottmann and S. Pokrant, *ChemSusChem*, 2019, **12**, 1931–1938.

111 A. Hankin, F. E. Bedoya-Lora, C. K. Ong, J. C. Alexander, F. Petter and G. H. Kelsall, *Energy Environ. Sci.*, 2017, **10**, 346–360.

112 I. Rodríguez-Gutiérrez, L. R. P. Peregrino, G. H. Morais, F. Coa, D. S. Teodoro Martinez, R. V. Gonçalves and F. L. Souza, *ACS Energy Lett.*, 2025, **10**, 4769–4776.

113 P. P. Kunturu, S. Bera, H. Johnson and M. N. Tsampas, *Artif. Photosynth.*, 2025, **1**, 106–116.

114 Y. An, C. Lin, C. Dong, R. Wang, J. Hao, J. Miao, X. Fan, Y. Min and K. Zhang, *ACS Energy Lett.*, 2024, **9**, 1415–1422.

115 K. Bienkowski, R. Solarska, L. Trinh, J. Widera-Kalinowska, B. Al-Anesi, M. Liu, G. K. Grandhi, P. Vivo, B. Oral, B. Yılmaz and R. Yıldırım, *ACS Catal.*, 2024, **14**, 6603–6622.

116 V.-H. Trinh and J. Seo, *ACS Sustainable Chem. Eng.*, 2023, **11**, 1655–1665.

117 J. Seo, S. Mun and V.-H. Trinh, *Inorg. Chem. Front.*, 2026, **13**, 51–62.

118 J. Seo and K. Domen, *Mater. Chem. Front.*, 2024, **8**, 1451–1479.

119 A. Kumar, A. Kumar and V. Krishnan, *ACS Catal.*, 2020, **10**, 10253–10315.

120 X. Li, H. Zhao, J. Liang, Y. Luo, G. Chen, X. Shi, S. Lu, S. Gao, J. Hu, Q. Liu and X. Sun, *J. Mater. Chem. A*, 2021, **9**, 6650–6670.

121 X. Ma, J. Qu, L. Zhang, J. Ma, Y. Cao, K. Nie, Q. Ji, C. Wang, L. Ma and D. Jing, *Int. J. Hydrogen Energy*, 2024, **55**, 441–454.

122 X. Ma, Y. Gao, B. Yang, X. Lou, J. Huang, L. Ma and D. Jing, *Mater. Today Nano*, 2023, **21**, 100289.

123 Y. Jiang, S. Zhou, S. S. Mofarah, R. Niu, Y. Sun, A. Rawal, H. Ma, K. Xue, X. Fang, C. Y. Toe, W.-F. Chen, Y.-S. Chen, J. M. Cairney, R. Rahman, Z. Chen, P. Koshy, D. Wang and C. C. Sorrell, *Nano Energy*, 2023, **116**, 108830.

124 S. Navalón, A. Dhakshinamoorthy, M. Álvaro, B. Ferrer and H. García, *Chem. Rev.*, 2023, **123**, 445–490.

125 K. Sun, Y. Qian and H.-L. Jiang, *Angew. Chem., Int. Ed.*, 2023, **62**, e202217565.

126 B. Singh and S. Verma, *Mater. Chem. Front.*, 2024, **8**, 3136–3149.

127 W.-Y. Chen, Y.-A. Yang and I.-W. P. Chen, *Chem. Eng. J.*, 2025, **520**, 166045.

128 M. Jothi, P. Gnanasekar, B. S. Ooi and J. Kulandaivel, *J. Phys. Chem. C*, 2024, **128**, 12799–12807.

129 H. Liu, P. Fu, D. Cui, A. Yuan, H. Zhang, J. Du, Y. Cheng, G. Wang, X. Yang and L. Chen, *J. Colloid Interface Sci.*, 2026, **703**, 139234.

130 Y. Bao, H. Ru, Y. Wang, K. Zhang, R. Yu, Q. Wu, A. Yu, D.-S. Li, C. Sun, W. Li and J. Tu, *Adv. Funct. Mater.*, 2024, **34**, 2314611.

131 D. Xie, J. Wang, B. Huang, Y. Yang, D. Lin, C. Xu and F. Xie, *CrystEngComm*, 2025, **27**, 678–686.

132 J. Li, S. Sun, N. Gao, H. Li, K. Liang, J. Hai, S. He, X. Mu and B. Wang, *Nanoscale Adv.*, 2023, **5**, 3527–3535.

133 L. Li, Z. Zhou, L. Li, Z. Zhuang, J. Bi, J. Chen, Y. Yu and J. Yu, *ACS Sustainable Chem. Eng.*, 2019, **7**, 18574–18581.

134 Q. Yue, G. Li, P. Fu, B. Meng, F. Ma, Y. Zhou and J. Wang, *Nano Res.*, 2023, **16**, 6251–6259.

135 C.-L. Chang, T.-F. Huang, W.-C. Lin, L.-Y. Ting, C.-H. Shih, Y.-H. Chen, J.-J. Liu, Y.-T. Lin, Y.-T. Tseng, Y.-H. Wu, Y.-E. Sun, M. H. Elsayed, C.-W. Chen, C.-H. Yu and H.-H. Chou, *Adv. Energy Mater.*, 2023, **13**, 2300986.

136 Q. Yue, Z. Zhang, X. Liu, C. Zhu, Y. Wen, P. Fu, Q. Hu, X. Qu, Y. Zhou and J. Wang, *Chem. Eng. J.*, 2025, **507**, 160481.

137 X. Zhang, M. Chang, D. Wang, L. Wang, X. Yang, Z. Ben, Q. Zhang and Y. Lu, *J. Colloid Interface Sci.*, 2025, **682**, 1151–1163.

138 J. Zhang, X. Li, J. Chang, P. She, H. Li, S. Qiu and Q. Fang, *Angew. Chem., Int. Ed.*, 2025, e19752.

139 S. Xiao, D. Wan, K. Zhang, H. Qu and J. Peng, *J. Environ. Sci.*, 2016, **50**, 103–108.

140 Y. Zhang, Y. Ji, J. Li, J. Bai, S. Chen, L. Li, J. Wang, T. Zhou, P. Jiang, X. Guan and B. Zhou, *J. Hazard. Mater.*, 2021, **402**, 123725.

141 F. Li, L. Sun, Y. Liu, X. Fang, C. Shen, M. Huang, Z. Wang and D. D. Dionysiou, *J. Hazard. Mater.*, 2020, **400**, 123246.

142 X. Zhang, W. Li, X. Gong, W. Fan and P. Ren, *Desalin. Water Treat.*, 2015, **54**, 1003–1012.

143 Y. Ji, J. Bai, J. Li, T. Luo, L. Qiao, Q. Zeng and B. Zhou, *Water Res.*, 2017, **125**, 512–519.

144 Z. Yan, Z. Dai, W. Zheng, Z. Lei, J. Qiu, W. Kuang, W. Huang and C. Feng, *Water Res.*, 2021, **205**, 117678.

145 Y. Zhang, J. Li, J. Bai, L. Li, S. Chen, T. Zhou, J. Wang, L. Xia, Q. Xu and B. Zhou, *Environ. Sci. Technol.*, 2019, **53**, 6945–6953.

146 Z. Shen, Y. Zhang, C. Zhou, J. Bai, S. Chen, J. Li, J. Wang, X. Guan, M. Rahim and B. Zhou, *Water Res.*, 2020, **170**, 115357.

147 J. E. Grebel, J. J. Pignatello and W. A. Mitch, *Environ. Sci. Technol.*, 2010, **44**, 6822–6828.

148 X. Zhang, A. Hu, C. Pan, Q. Zhao, X. Wang and J. Lu, *Org. Process Res. Dev.*, 2013, **17**, 1591–1596.

149 J. Wang, R. Li, D. Zeng, W. Wang, Y. Zhang, L. Zhang and W. Wang, *Chem. Eng. J.*, 2023, **452**, 139505.

150 S. J. Freakley, N. Dimitratos, D. J. Willock, S. H. Taylor, C. J. Kiely and G. J. Hutchings, *Acc. Chem. Res.*, 2021, **54**, 2614–2623.

151 L. A. Hull, W. P. Giordano, D. H. Rosenblatt, G. T. Davis, C. K. Mann and S. B. Milliken, *J. Phys. Chem.*, 1969, **73**, 2147–2152.

152 W. H. Dennis, L. A. Hull and D. H. Rosenblatt, *J. Org. Chem.*, 1967, **32**, 3783–3787.

153 E. E. van Tamelen, V. B. Haarstad and R. L. Orvis, *Tetrahedron*, 1968, **24**, 687–704.

154 W. E. Pereira, Y. Hoyano, R. E. Summons, V. A. Bacon and A. M. Duffield, *Biochim. Biophys. Acta, Gen. Subj.*, 1973, **313**, 170–180.

155 V. C. Hand, M. P. Snyder and D. W. Margerum, *J. Am. Chem. Soc.*, 1983, **105**, 4022–4025.

156 T. Stelmaszyńska and J. M. Zgliczynski, *Eur. J. Biochem.*, 1978, **92**, 301–308.

157 C. L. Hawkins and M. J. Davies, *J. Chem. Soc., Perkin Trans. 2*, 1998, 1937–1946.

158 Z. T. How, K. L. Linge, F. Busetti and C. A. Joll, *Environ. Sci. Technol.*, 2017, **51**, 4870–4876.

159 T. Ding, L. Long, M.-J. Yuan, W. Xu, S.-Y. Wong, H. Gao, Y.-H. Wang, Y.-Y. Yeung and X. Jiang, *J. Am. Chem. Soc.*, 2025, **147**, 16225–16236.

160 P.-F. Biard, A. Couvert, C. Renner and J.-P. Levasseur, *Can. J. Chem. Eng.*, 2010, **88**, 682–687.

161 M. Azizi, P.-F. Biard, A. Couvert and M. Ben Amor, *Chem. Eng. Res. Des.*, 2015, **94**, 141–152.

162 M. Whiteman, N. S. Cheung, Y.-Z. Zhu, S. H. Chu, J. L. Siau, B. S. Wong, J. S. Armstrong and P. K. Moore, *Biochem. Biophys. Res. Commun.*, 2005, **326**, 794–798.

163 X. L. Armesto, M. Canle, M. I. Fernandez, M. V. Garcia and J. A. Santaballa, *Tetrahedron*, 2000, **56**, 1103–1109.

164 J. Ra, J. Tolu, D. Rentsch, T. Manasfi and U. von Gunten, *Water Res.*, 2025, **270**, 122806.

165 Y. Hu, G. Xie and D. M. Stanbury, *Inorg. Chem.*, 2017, **56**, 4047–4056.

166 G. Ding, C. Li, Y. Ni, L. Chen, L. Shuai and G. Liao, *EES. Catal.*, 2023, **1**, 369–391.

167 Y.-Y. Li, J.-S. Fan, R.-Q. Tan, H.-C. Yao, Y. Peng, Q.-C. Liu and Z.-J. Li, *ACS Appl. Mater. Interfaces*, 2020, **12**, 54507–54516.

168 L. Hao, L. Kang, H. Huang, L. Ye, K. Han, S. Yang, H. Yu, M. Batmunkh, Y. Zhang and T. Ma, *Adv. Mater.*, 2019, **31**, 1900546.

169 W. Zhang, W. Ma, Y. Ma, P. Chen, Q. Ye, Y. Wang, Z. Jiang, Y. Ou and F. Dong, *Nano Mater. Sci.*, 2024, **6**, 235–243.

170 D.-Y. Kuo, H. Paik, J. N. Nelson, K. M. Shen, D. G. Schlom and J. Suntivich, *J. Chem. Phys.*, 2019, **150**, 041726.

171 S. Saha, P. Gayen and V. K. Ramani, *ChemCatChem*, 2020, **12**, 4922–4929.

172 A. R. Zeradjanin, N. Menzel, P. Strasser and W. Schuhmann, *ChemSusChem*, 2012, **5**, 1897–1904.

173 I. E. Wachs, *Catal. Today*, 1996, **27**, 437–455.

174 Y. Krockenberger, J. Ruiters, H. Irie, Y. Taniyasu and H. Yamamoto, *J. Phys. Chem. C*, 2025, **129**, 18157–18163.

175 Y. Ping, G. Galli and W. A. I. Goddard, *J. Phys. Chem. C*, 2015, **119**, 11570–11577.

176 K. S. Exner, *ChemElectroChem*, 2020, **7**, 1448–1455.

177 D.-Y. Kuo, H. Paik, J. Kloppenburg, B. Faeth, K. M. Shen, D. G. Schlom, G. Hautier and J. Suntivich, *J. Am. Chem. Soc.*, 2018, **140**, 17597–17605.

178 K. S. Exner, *Phys. Chem. Chem. Phys.*, 2020, **22**, 22451–22458.

179 K. S. Exner, *J. Phys. Chem. C*, 2019, **123**, 16921–16928.

180 K. S. Exner, J. Anton, T. Jacob and H. Over, *Angew. Chem., Int. Ed.*, 2014, **53**, 11032–11035.

181 C. E. Finke, S. T. Omelchenko, J. T. Jasper, M. F. Lichterman, C. G. Read, N. S. Lewis and M. R. Hoffmann, *Energy Environ. Sci.*, 2019, **12**, 358–365.

182 H. Gong, B. Zhu, D. Zhang, T. Liu, P. Kuang and J. Yu, *Appl. Catal., B*, 2024, **349**, 123892.

183 M. Teranishi, R. Hoshino, S. Naya and H. Tada, *Angew. Chem., Int. Ed.*, 2016, **55**, 12773–12777.

184 S. Sun, L. He, M. Yang, J. Cui and S. Liang, *Adv. Funct. Mater.*, 2022, **32**, 2106982.

185 D. Chen, C.-L. Dong, Y. Zou, D. Su, Y.-C. Huang, L. Tao, S. Dou, S. Shen and S. Wang, *Nanoscale*, 2017, **9**, 11969–11975.

186 Y. Yan, C. Liu, H. Jian, X. Cheng, T. Hu, D. Wang, L. Shang, G. Chen, P. Schaaf, X. Wang, E. Kan and T. Zhang, *Adv. Funct. Mater.*, 2021, **31**, 2009610.

187 F. T. Haase, A. Bergmann, T. E. Jones, J. Timoshenko, A. Herzog, H. S. Jeon, C. Rettenmaier and B. R. Cuenya, *Nat. Energy*, 2022, **7**, 765–773.

188 Z. Li, L. Luo, M. Li, W. Chen, Y. Liu, J. Yang, S.-M. Xu, H. Zhou, L. Ma, M. Xu, X. Kong and H. Duan, *Nat. Commun.*, 2021, **12**, 6698.

189 Y. Chen and L. Zhang, *Appl. Catal., B*, 2024, **347**, 123768.